

Geophysical and atmospheric implications of $f\text{O}_2$ -dependent melting on rocky exoplanets

Mariana Sastre^{1*}, Tim Lichtenberg¹, Laurent Soucasse^{2,3}, Dan J. Bower⁴, Harrison Nicholls⁵, Inga Kamp¹

¹ Kapteyn Astronomical Institute, University of Groningen, Groningen, The Netherlands

² Netherlands eScience Center, Amsterdam, The Netherlands

³ Interuniversity Micro Electronics Centre, Leuven, Belgium

⁴ Institute of Geochemistry and Petrology, Department of Earth and Planetary Sciences, ETH Zürich, Zürich, Switzerland

⁵ Institute of Astronomy, University of Cambridge, Cambridge, United Kingdom

ABSTRACT

The geochemical evolution of long-lived magma oceans is strongly regulated by volatile exchange between the molten mantle and the atmosphere. For planets inside the runaway-greenhouse limit, this coupled evolution can persist for billions of years, governing bulk density, surface conditions, and long-term geodynamics. However, most existing studies assume Earth-like (oxidized) conditions and neglect the influence of redox state on melt thermodynamics and volatile release. We quantified how experimentally derived, oxygen-fugacity-dependent melting curves implemented within the coupled interior-atmosphere framework PROTEUS propagate into the thermal structure, melt fraction, and rheological evolution of rocky exoplanet interiors, applying this to the short-period super-Earth GJ 1132 b. We found strongly non-linear thermal responses to variations in melting curves. In volatile-poor systems, reduced melting curves ($f\text{O}_2 \leq \text{IW}$, where IW denotes the iron-wüstite buffer) promote earlier deep-mantle crystallisation relative to oxidised (IW+2.0) and Earth-like (IW+4.0) cases (range IW−4.0 to IW+4.0), favouring late-stage surface magma oceans sustained by greenhouse warming, while oxidized melting curves maintain higher melt fractions and a vertically extended magma ocean. Reduced mantles produce massive H_2 -CO-rich atmospheres; oxidized mantles favour thinner H_2O -CO₂ envelopes. In volatile-rich systems, the interior reaches radiative equilibrium at high melt fractions, sustaining a steady-state global magma ocean in which melting curve variations do not significantly influence solidification timing. This indicates a hierarchical control: volatile inventory and surface oxygen fugacity act as the primary regulators of thermal state, while oxygen-fugacity-dependent melting relations provide a secondary modulation. These contrasting regimes produce distinct atmospheric compositions and formation timescales, offering testable spectral predictions for close-in rocky exoplanets evaluable with forthcoming JWST observations.

Key words. planets and satellites: interiors – planets and satellites: atmospheres – planets and satellites: composition – planets and satellites: terrestrial planets – planets and satellites: physical evolution

1. Introduction

Planetary formation is thought to proceed through various stages of accretion by impacts of planetesimals and the accretion of pebbles within the protoplanetary disc (Johansen & Lambrechts 2017; Raymond et al. 2020; Batygin & Morbidelli 2023). The timescales and initial heat budget at which this process occurs imply a significant amount of energy, enough to induce multiple episodes of large-scale mantle melting. This stage is known as the magma ocean phase (Elkins-Tanton 2012). As the magma ocean cools and crystallizes, some fraction of the volatile content dissolved within the planet’s interior is outgassed to the exterior, contributing to the growth and composition of a secondary atmosphere and initiating long-term climate evolution (Elkins-Tanton 2008; Lebrun et al. 2013; Hamano et al. 2013; Bower et al. 2019, 2022; Salvador et al. 2023; Lichtenberg et al. 2023; Nicholls et al. 2024; Boukaré et al. 2025). The outgassed atmosphere strongly influences the crystallisation of the magma ocean. By producing a greenhouse blanketing effect, it retains heat and can keep surface temperatures above the solidus temperature, which is the threshold for melting under given thermodynamic and compositional conditions. This helps maintain a molten surface and extends the lifetime of the magma ocean.

(Abe & Matsui 1985, 1988; Schaefer et al. 2016; Salvador et al. 2017; Lichtenberg et al. 2021).

Previous studies (Elkins-Tanton 2008; Lebrun et al. 2013) showed that volatile species exhibit contrasting partitioning behaviour during magma ocean evolution. Owing to its low solubility in silicate melts, carbon-bearing species preferentially reside in the atmosphere, being efficiently outgassed from the earliest stages of crystallisation (Bower et al. 2022). In contrast, the higher solubility of H_2O causes it to remain largely dissolved in the melt, favouring retention within the interior until the final stages of solidification (Suer et al. 2023; Sossi et al. 2023; Bower et al. 2022, 2025). Water-rich atmospheres enhance thermal blanketing and suppress radiative cooling, extending the molten phase. Therefore, the initial water inventory plays a key role in setting magma ocean lifetimes. In contrast, atmospheres dominated by carbon-bearing species (e.g., CO_2 , CO), are generally more transparent to outgoing longwave radiation and therefore less effective at retaining heat (Kiehl & Trenberth 1997; Salvador et al. 2023). Stellar evolution can produce a similar effect, as high stellar irradiation may suppress efficient cooling through atmospheric buffering of infrared emission, potentially sustaining long-lived magma oceans. However, recent studies indicate that this behaviour is not governed by a universal critical flux threshold but depends more on atmospheric and interior proper-

* Corresponding author: m.c.villamil.sastre@rug.nl

ties (Hamano et al. 2013, 2015; Salvador et al. 2017; Boer et al. 2025).

Exoplanet surveys provide an opportunity to test models of coupled interior–atmosphere evolution during magma ocean phases (Kreidberg & Stevenson 2025; Lichtenberg et al. 2025). Recent JWST observations have transformed our understanding of rocky ultra-short-period exoplanets, revealing that some retain volatile secondary atmospheres rather than being entirely desiccated. Using JWST/NIRCam and MIRI observations, Hu et al. (2024) detected a persistent volatile envelope around 55 Cnc e, inconsistent with a bare-rock or silicate-vapour atmosphere and likely dominated by CO or CO₂. Similarly, Teske et al. (2025) reported the dayside emission spectrum of TOI-561 b, whose brightness temperatures require a thick atmosphere that redistribute heat away from the planet’s dayside. These results provide the first evidence that volatile-rich envelopes can survive on highly irradiated rocky planets. Because these highly irradiated planets exist at thermodynamic conditions that may favour persistent dayside or global magma ocean regimes, these detections open a new avenue for linking observable secondary atmospheres to their geochemical histories. Therefore, interpreting these observations requires a detailed understanding of the coupled evolution of planetary interiors and atmospheres, and of the processes that regulate volatile release and retention.

Although atmospheric processes have received substantial attention, the geochemical and geophysical evolution of the interior is equally important in shaping a planet’s long-term climate and thermodynamic state. A key factor in this evolution is the oxidation state of the silicate mantle, which influences melting behaviour, volatile speciation, and interior–atmosphere exchange (Hirschmann 2012; Lichtenberg et al. 2021; Gaillard et al. 2022; Wordsworth & Kreidberg 2022; Salvador et al. 2023; Nicholls et al. 2024). The mantle redox state reflects the equilibrium distribution of electrons among multivalent elements, particularly the balance between Fe²⁺ and Fe³⁺ in silicate phases (Cottrell et al. 2025). Controlled by the oxygen chemical potential, this thermodynamic state is commonly quantified by the oxygen fugacity, fO_2 , which represents the thermodynamic availability of oxygen for redox reactions, even in the absence of free molecular oxygen (Wade & Wood 2005; Kasting 2014; Salvador et al. 2023). High oxygen fugacity corresponds to more oxidizing mantle conditions, whereas low oxygen fugacity favours reduced chemical species.

As the dominant multivalent species in the mantle, iron simultaneously records and controls redox conditions through the balance of its oxidation states (Salvador et al. 2023). The oxygen fugacity of a system is set by equilibrium among coexisting redox-sensitive phases, which buffer the chemical potential of oxygen at specific conditions. These equilibrium reactions define reference oxygen fugacity states that are commonly referred to as redox buffers (Frost & McCammon 2008; Hirschmann 2012; Cottrell et al. 2025). One of the most commonly used redox buffer is the iron–wüstite (IW) buffer Eq. 1., which represents the equilibrium between metallic iron (Fe) and ferrous iron incorporated in wüstite (FeO, iron(II) oxide). The oxygen fugacity relative to this buffer is expressed in log units as $\Delta \log fO_2(IW) = \log fO_2 - \log fO_2^{IW}$, where fO_2^{IW} is the oxygen fugacity at the IW equilibrium at the same pressure and temperature.



This buffer is characteristic of moderately reducing conditions in planetary interiors. With higher relative fO_2 correspond-

ing to greater stabilization of oxidized iron species and lower values favouring metallic iron and more reducing conditions (Salvador et al. 2023).

Previous studies have shown that oxygen fugacity and crystallisation regimes jointly regulate the thermal and chemical evolution of planetary magma oceans (O’Neill & Eggins 2002; Armstrong et al. 2015; Sossi et al. 2020; Lichtenberg et al. 2021; Bower et al. 2022; Gaillard et al. 2022; Shorttle et al. 2024; Nicholls et al. 2024). Under reducing conditions relative to the IW buffer, coupled interior–atmosphere models predict C- and H-rich atmospheres dominated by H₂ and CO, whereas oxidizing conditions favour H₂O- and CO₂-dominated compositions. CO remains stable across a wide redox range.

Complementary to these redox-driven trends, melt–solid separation modulates evolution (Boukaré et al. 2025). For instance, Bower et al. (2022) showed that fractional crystallisation (crystal segregation) and equilibrium crystallisation (no crystal segregation) lead to different melt redistribution, affecting the timing of cooling and outgassing processes.

In addition, redox-dependent changes in atmospheric speciation influence radiative properties and thermal evolution. For example, by treating fO_2 as a free parameter, Nikolaou et al. (2019); Katyal et al. (2020) showed that changes in the oxidation state modify the equilibrium between interior and atmosphere, alter volatile partitioning, and modulate the outgoing radiative flux, thereby shaping planetary cooling. At the same time, reducing conditions can favour the formation of thick H₂-rich atmospheres that, at sufficiently high pressures, also enhance greenhouse blanketing and prolong magma-ocean cooling times (Pierrehumbert & Gaidos 2011; Lichtenberg et al. 2021; Nicholls et al. 2024). When volatile species such as sulphur are included, the redox state further controls the emergence of H-C versus C-N-S-dominated atmospheric compositions (Gaillard et al. 2022).

However, most existing models consider volatile inventories dominated by H₂O and CO₂ (Lebrun et al. 2013; Salvador et al. 2017; Hier-Majumder & Hirschmann 2017; Wordsworth et al. 2018; Nikolaou et al. 2019; Barth et al. 2021) H₂O (Hamano et al. 2015; Schaefer et al. 2016), or H₂O, CO₂, and O₂ (Krissansen-Totton et al. 2021). In parallel, coupled frameworks linking radiative–convective atmospheres with vertically resolved mantle evolution have also been developed (Lichtenberg et al. 2021). Their model included seven atmospheric species (H₂, H₂O, CO₂, CH₄, CO, O₂, and N₂) and simulated the coupled evolution of the magma ocean solidification, and the resulting atmospheric spectral signatures. From these simulations, Lichtenberg et al. (2021) showed that atmospheric composition strongly controls cooling timescales, with H₂-dominated atmospheres producing the longest-lived magma oceans.

More recently, fully coupled models have emerged that include the regulation of the atmospheric inventory through feedbacks between the interior and atmosphere, and compute volatile outgassing and atmospheric composition during magma-ocean evolution. These feedbacks arise from the coupled thermal evolution, whereby interior melting and degassing influence atmospheric opacity and cooling, which in turn affect the rate of interior solidification (Krissansen-Totton et al. 2021, 2024; Nicholls et al. 2024), these studies were compiled and reviewed by Lichtenberg & Miguel (2025); Lichtenberg et al. (2026).

Collectively, these studies demonstrate that the oxidation state of the magma ocean strongly controls planetary thermal evolution and atmospheric composition. As long as the magma ocean remains in equilibrium with the atmosphere and the mantle volatile reservoir greatly exceeds that of the atmosphere, the interior composition effectively buffers the atmospheric re-

dox state. Recent work (Walbecq et al. 2025) suggests that outgassing may be limited by dynamical constraints on volatile exsolution and transport, so interior–atmosphere equilibrium is not guaranteed during magma ocean solidification. Delayed degassing can therefore accelerate cooling and alter both atmospheric composition and mantle redox evolution. Regardless of outgassing efficiency, the mantle’s baseline redox state is inherited from high-pressure differentiation, set by equilibrium between metallic iron and iron oxide (Wade & Wood 2005; Schlichting & Young 2022; Young et al. 2023; Schaefer et al. 2024; Cottrell et al. 2025). Core-formation models further indicate that Earth’s mantle ended accretion in a relatively reduced state, around IW–2.0 i.e. two log units above the iron–wüstite buffer (Badro et al. 2015; Rubie et al. 2015).

Nevertheless, following Hirschmann (2012), recent experiments and molecular dynamics simulations suggested that high pressures may stabilize ferric (Fe^{3+}) over ferrous (Fe^{2+}) iron in silicate melts (Zhang et al. 2017; Armstrong et al. 2019; Deng et al. 2020; Kuwahara et al. 2023; Schaefer et al. 2024). As a result, silicate melts equilibrated at depth may contain non-negligible fractions of ferric iron even under globally reducing conditions. During core formation, the segregation of metallic iron implies that a well-mixed mantle inherits the elevated Fe^{3+}/Fe^{2+} ratios established at high pressure, resulting in higher effective oxidation states at lower pressures (Hirschmann 2022; Schaefer et al. 2024).

Chemical partitioning during magma ocean evolution further modifies mantle oxidation. Fractional crystallisation enriches FeO in the residual melt (Elkins-Tanton et al. 2003; Elkins-Tanton 2008; Boukaré et al. 2018; Maurice et al. 2024), potentially forming a dense, iron-rich layer that can trigger mantle overturn (Elkins-Tanton et al. 2003; Boukaré et al. 2015, 2018). Because ferric iron (Fe^{3+}) is moderately incompatible relative to ferrous iron (Fe^{2+}) (Canil & O’Neill 1996; Sorbadere et al. 2018), crystallisation drives their fractionation (McCanta et al. 2009). This redistribution establishes evolving redox gradients, linking interior differentiation to the oxidation state of surface volatiles (Hirschmann 2012; Sossi et al. 2020).

Beyond its role in volatile and redox exchange, fO_2 also directly modifies the melting behaviour of the mantle. In this work, we distinguished between two physically distinct oxidation states: a deep-mantle oxygen fugacity, fO_2^{melt} , which governs melting behaviour at high pressure, and a surface oxygen fugacity, fO_2^{surf} , which controls near-surface outgassing and volatile speciation. This distinction reflects an effective pressure-dependence of fO_2 , consistent with experimental and theoretical results indicating that oxidation state may vary between deep and shallow mantle conditions. Recent experiments by Lin et al. (2024) suggested that increasing fO_2^{melt} depresses the solidus relative to reduced baseline measurements (Trønnes 2000; Trønnes & Frost 2002; Ishii et al. 2018). This effect is attributed to increased Fe^{3+} concentrations in the melt, which act as incompatible species that lower the activities of major cation-bearing components and thermodynamically stabilize the liquid phase relative to crystalline minerals. As a result, oxidizing conditions can significantly depress the solidus by hundreds of Kelvin across a broad pressure range highlighting the combined influence of melt composition and pressure on magma ocean stability (Shahar et al. 2021; Lin et al. 2024). This redox-dependent shift in the melting curves influences where a planetary interior temperature profile intersects the solidus, thereby affecting the onset of crystallisation, the depth and longevity of the magma ocean, and the efficiency of volatile exchange between the interior and the growing atmosphere. In principle, increasing fO_2 should shift

melting curves to lower temperatures, allowing melting to persist to greater depths and potentially prolonging magma-ocean lifetimes, whereas more reducing conditions would be expected to favour earlier crystallisation.

In addition to the effects of oxygen fugacity, dissolved volatiles also modify mantle melting relations. Experimental studies indicate that H_2O and CO_2 can significantly depress silicate melting temperatures by altering melt structure and phase relations. In particular, water promotes hydroxylation of the silicate network (Katz et al. 2003), whereby H_2O is incorporated into the melt as OH^- , weakening the mineral framework and stabilizing the liquid phase. This volatile-induced modification of melt properties lowers the solidus and can influence the thermal evolution and longevity of magma oceans (Dasgupta & Hirschmann 2007; Myhill et al. 2017; Xie et al. 2024). However, explicitly resolving how evolving volatile contents feedback on mantle melting introduces additional complexity that lies beyond the scope of the present study.

In this work, we extended the PROTEUS simulation framework (Lichtenberg et al. 2021; Nicholls et al. 2024, 2025a,b; Nicholls 2026) to quantify the influence of redox-dependent melting relations and volatile speciation on the coupled thermal and compositional evolution of magma ocean planets. We explicitly distinguished between the deep-mantle oxidation state, fO_2^{melt} , which governs melting behaviour and interior cooling, and the surface oxidation state, fO_2^{surf} , which regulates outgassing and atmospheric composition. As a reference case, we adopted the super-Earth exoplanet GJ 1132 b, discovered by Berta-Thompson et al. (2015) using the MEarth-South telescope array. It orbits a nearby M dwarf star at 12.04 pc, with a mass of $1.62 \pm 0.55 M_{\oplus}$, a radius of $1.16 \pm 0.11 R_{\oplus}$, and a bulk density of $6.0 \pm 2.5 \text{ g cm}^{-3}$, consistent with a rocky composition (Southworth et al. 2017). Receiving approximately 19 times Earth’s insolation, it represents a benchmark target for testing magma ocean and atmospheric evolution models under strong stellar irradiation. With $T_{\text{eq}} \approx 584 \text{ K}$ and $A_B = 0.19^{+0.12}_{-0.15}$ (Xue et al. 2024), its atmospheric characterisation history includes previously claimed detections of H_2O , CH_4 and H_2 -dominated envelopes (Southworth et al. 2017; Swain et al. 2021; May et al. 2023). More recent and higher-precision JWST observations have progressively converged toward a bare-rock interpretation (Xue et al. 2024; Bennett et al. 2025). We selected GJ 1132 b as our reference case because it combines well-characterised planetary parameters, favourable observational accessibility, and a stringent set of atmospheric constraints that can directly test the evolutionary pathways predicted by our models. Using this system, we investigated how variations in deep-mantle and surface redox reservoirs control mantle cooling history, solidification timescales, and volatile release. By systematically exploring different combinations of fO_2^{melt} and fO_2^{surf} together with the initial hydrogen inventory (H_{oceans}) inherited from accretion, we aim to quantify the geophysical conditions under which redox processes may leave detectable imprints on the secondary atmospheres of super-Earth exoplanets.

2. Methods

2.1. PROTEUS overview

To simulate the geophysical and atmospheric evolution of magma ocean exoplanets, we upgraded and employed the PROTEUS framework¹ in version 25.07.31 (Lichtenberg et al.

¹ <https://proteus-framework.org>

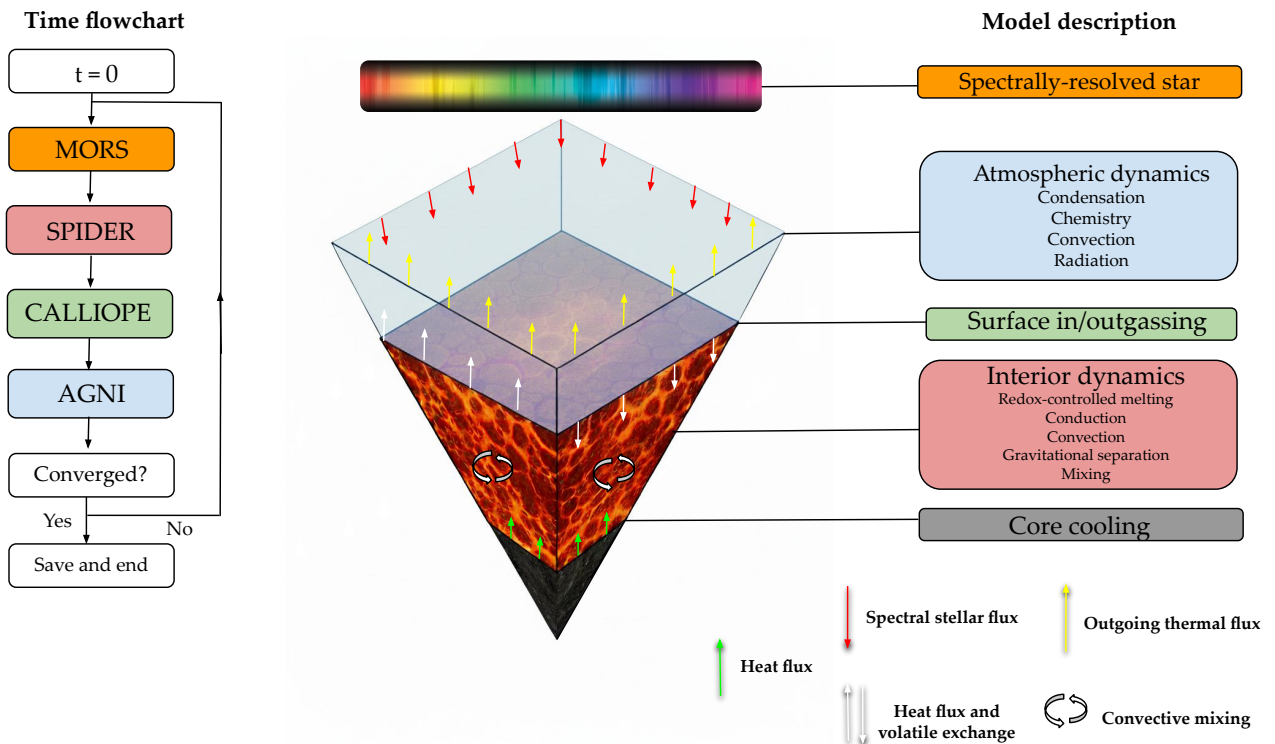


Fig. 1. Schematic overview of the PROTEUS framework and its time-integration workflow. The interior, surface volatile exchange, and radiative-convective atmosphere are solved as independent modules that iteratively exchange boundary conditions at each timestep. In the time-flowchart, each timestep proceeds by iterating the coupled modules until the surface fluxes, volatile inventories, and atmospheric structure converge to a self-consistent solution. If convergence is not achieved, the boundary conditions are iteratively updated until convergence of the coupled solution is reached. The colour-coding in the time-flowchart (left) corresponds to the module descriptions in the model diagram (right), where each coloured module in the flowchart solves the physical processes listed in its corresponding coloured box on the right.

2021; Nicholls et al. 2024, 2025a,b), a modular, self-consistent 1-D evolution code designed to track the coupled thermal and compositional history of rocky planets. PROTEUS is structured as a set of stand-alone but interdependent physical modules that simulates: interior, atmospheric energy transport, escape to space, stellar evolution, and outgassing that communicate through shared boundary conditions (Nicholls 2026). At each interior timestep, energy, mass, and compositional fluxes are iteratively exchanged between modules until convergence of the coupled solution is achieved. The interior evolves forward in time, while the atmosphere is solved in quasi-steady state and responds instantaneously to evolving boundary conditions. This enables the model to track planets from an initially molten state through crystallisation and volatile exchange between mantle and atmosphere, resolving equilibrium states at each timestep and the hysteresis that emerges from coupled atmospheric-interior feedbacks (Lichtenberg et al. 2025, 2026; Nicholls et al. 2025a).

In this work, we advanced simulations until one of several termination criteria is met: (i) whole-mantle melt fraction decreases below a critical threshold $\phi < 0.05$, indicating solidification; (ii) the system reaches global energy balance, where the melt fraction becomes constant in time and the net radiative flux between the interior-atmosphere is negligible ($\lesssim 1 \text{ W m}^{-2}$); or (iii) a maximum integration time is reached (set to 200 Myr). This upper limit was chosen because the key phases of magma ocean evolution, including rapid crystallisation and convergence toward long-lived equilibrium states, occur within the first 10–100 Myr (Nicholls et al. 2024). Our focus is therefore on the

early thermochemical evolution of the planet, and we do not attempt to model the subsequent long-term solid-state or tectonic evolution beyond this stage.

Figure 1 summarizes this workflow by showing how PROTEUS cycles through its modular components until convergence is achieved at each time step. In this study, we primarily modified the interior module (SPIDER) to incorporate redox-dependent melting relations, while the atmospheric, stellar evolution and volatile exchange modules follow previous implementations and are therefore only briefly described below.

2.2. Stellar evolution model

Within the PROTEUS framework, the temporal evolution of stellar irradiation is modelled using the MORS stellar evolution code, originally developed by Johnstone et al. (2021). MORS models stars as coupled rotating shells surrounding a homogeneous core, allowing it to self-consistently calculate angular momentum transport and rotational spin-down over time. Since stellar activity and high-energy emission are closely linked to rotation, MORS then calculates the evolution of X-ray, extreme ultraviolet, and bolometric luminosities as a function of stellar mass, age, and initial rotation rate (Johnstone et al. 2021). These outputs are combined with empirical scaling relations to build the star’s evolving emission spectrum (Nicholls et al. 2024). The resulting time-dependent stellar fluxes are continuously updated and coupled to the interior and atmospheric modules of PROTEUS, enabling a self-consistent treatment of how changing stellar irradiation influences planetary climate, chemistry, and in-

terior–atmosphere feedbacks throughout the planet’s evolution (Tsai et al. 2021; Pierrehumbert 2010). In this case, we used the star with a 50th percentile of rotation speed for its mass and age (Gallet & Bouvier 2013).

2.3. Atmospheric model

The energy transport in the atmosphere is computed with the open-source code AGNI (Nicholls et al. 2024; Nicholls et al. 2025b,c), a radiative–convective model that calculates the net atmospheric energy flux as a function of volatile composition, installation flux, and the temperature at the atmosphere–mantle boundary (Nicholls et al. 2025b). We employed AGNI in a configuration such that the atmospheric temperature–pressure profiles are convective (adiabatic). Based on this structure, AGNI calculates spectrally resolved radiative fluxes using the SOCRATES code under the two-stream approximation (Edwards & Slingo 1996; Amundsen et al. 2016; Sergeev et al. 2023), with gas opacities from the DACE (Grimm & Heng 2015; Grimm et al. 2021) database and collision-induced absorption parametrised using HITRAN (Gordon et al. 2022). We assumed the atmosphere is isochemical at the outgassed composition (see below, Sect. 2.4), with eight main volatile species: H_2O , H_2 , CO_2 , CO , SO_2 , S_2 , N_2 , and CH_4 . We assumed that the total number of moles of each volatile element is conserved throughout the simulation and do not model atmospheric escape. Consistent with our maximum integration time of 200 Myr, we focused on the early coupled interior–atmosphere evolution and do not attempt to model long-term atmospheric loss or the subsequent evolution toward present-day conditions. The impact of this assumption is discussed in Sect. 4.

2.4. Outgassing model

The exchange of volatiles between the molten mantle and the atmosphere is handled by the CALLIOPE outgassing module, based on (Bower et al. 2022). This module applies mass conservation to solve for the C-H-O-N-S volatile partial surface pressures at thermochemical-solubility equilibrium at the magma ocean surface (Chase 1996; Bower et al. 2019; Shorttle et al. 2024; Nicholls et al. 2024). The corresponding abundances are computed based on their solubility and equilibrium between the melt phase and the atmosphere. During the evolution and without considering atmospheric escape, we conserved C-H-N-S and partitioned them between melt and atmosphere using solubility laws that depend on surface temperature, melt fraction, and imposed fO_2 (Bower et al. 2025). Oxygen is not tracked as a finite reservoir; instead fO_2 is prescribed (infinite-reservoir approximation), so the atmosphere may effectively draw on or return O to the mantle to satisfy stoichiometry (Bower et al. 2022).

2.5. Interior model

The planetary interior is modelled using the SPIDER code (Bower et al. 2018, 2019), which simulates the thermal evolution of a magma ocean as it transitions from a fully molten state to partial or complete solidification. The model solves the vertically resolved energy balance using an entropy-based formulation of the conservation equation. The full numerical interior framework and implementation are described in detail in Bower et al. (2018), and have been adopted in previous PROTEUS studies. Here, we briefly summarise the key aspects of the interior

model, as our work focuses on how interior thermodynamics and melting behaviour influence atmospheric evolution.

In this context, the thermal evolution of the mantle is governed by the integral form of the energy conservation equation expressed in terms of entropy:

$$\int_V \rho T \frac{\partial S}{\partial t} dV = - \int_A \mathbf{F} \cdot \mathbf{n} dA + \int_V \rho H dV \quad (2)$$

with S specific entropy, ρ density, T temperature, F heat flux vector, n unit normal vector to the surface, H internal heat generation per unit mass, t time, and V volume. The model takes into account conduction, mixing, gravitational separation and convection as energy transport mechanism, which contribute to the total flux F . Convective heat flux is computed through mixing length theory, enabling this mechanism to be represented as a diffusive 1D process (Wagner et al. 2019). In this work, we adopted a constant mixing length parametrization, following the framework explored in Bower et al. (2018). In this way, the eddy diffusivity (κ_h) scales with a characteristic velocity depending on the local Reynolds number (Abe 1995; Stothers & Chin 1997), and affects the convective heat flux:

$$F_{\text{conv}} = -\rho T \kappa_h \frac{\partial S}{\partial r}. \quad (3)$$

Energy transport contribution due to gravitational separation only occurs in the mixed phase region, by permeable flow of melt from the solid background, and depends on the flow mechanism (crystal settling or flotation),

$$F_{\text{grav}} = a_g^2 g \rho (\rho_{\text{liq}} - \rho_{\text{sol}}) \zeta_{\text{grav}}(\phi) T \Delta S_{\text{fus}} / \eta_m. \quad (4)$$

where a_g is the grain size, η_m is the melt viscosity, ρ_{liq} and ρ_{sol} are the melt and solid densities at the liquidus and solidus, respectively, $\Delta S_{\text{fus}} = S_{\text{liq}} - S_{\text{sol}}$ is the entropy of fusion defined as the difference between liquid and solid entropies and $\zeta_{\text{grav}}(\phi)$ which parametrizes the dependence of the flow law on melt fraction ϕ , and accounts for the transition from crystal-rich suspensions at high melt fractions to porous flow at low melt fractions (Abe & Matsui 1988; Bower et al. 2018).

Phase mixing quantifies the energy transport carried by the latent heat which is released/absorbed as crystals form/melt while they are being transported through the solidifying mantle,

$$F_{\text{mix}} = -\rho T \Delta S_{\text{fus}} \kappa_h \frac{\partial \phi}{\partial r}, \quad (5)$$

We considered a single-component system with two phases (solid and liquid), such that the melting region is represented by a finite interval between the solidus and liquidus. In SPIDER, these melting curves are implemented through entropy–pressure lookup tables that define the boundaries of this two-phase region. Because SPIDER solves the conservation of energy in terms of specific entropy, all thermodynamic quantities including temperature are obtained from tables $T(S, P)$ and associated properties. At each pressure, the liquidus and solidus entropies ($S_l(P)$, $S_s(P)$) determine the local melt fraction, which is computed as a linear function of entropy between these bounds (Eq. 6). This representation allows SPIDER to flexibly incorporate melting relations from experimental petrology (e.g., peridotite and chondritic solidus/liquidus data) and to smoothly transition material properties across phase boundaries using numerical smoothing routines (Bower et al. 2018). Therefore, the lookup tables encode the full thermodynamic structure of the

melting region and directly determine where the mantle is solid, partially molten, or fully liquid such that

$$\phi = \begin{cases} 1, & \text{if } S > S_l \\ \frac{S - S_s}{S_l - S_s}, & \text{if } S_l \geq S \geq S_s \\ 0, & \text{if } S_s > S \end{cases} \quad (6)$$

Conduction is described by Fourier's law, with thermal diffusivity κ_t , specific heat capacity c and the adiabatic temperature gradient $(\partial T/\partial r)_S$, and is expressed as

$$F_{\text{cond}} = -\rho T \kappa_t \left(\frac{\partial S}{\partial r} \right) - \rho c \kappa_t \left(\frac{\partial T}{\partial r} \right)_S. \quad (7)$$

The total heat flux is expressed as the sum of the contributions of each heat flux associated to heat transport processes during the transition of a molten mantle:

$$F_{\text{total}} = F_{\text{conv}} + F_{\text{mix}} + F_{\text{cond}} + F_{\text{grav}}. \quad (8)$$

At each grid cell F_{total} can be positive or negative, defining the cooling or heating trajectory of individual layers within the planet's interior. Therefore, each of the fluxes will have a fundamental contribution to the total heat budget of the planet.

We do not directly model the geophysical evolution of the metallic core, and we assumed the core-mantle boundary (CMB) to be thermally coupled to the mantle based on energy balance such that

$$\frac{dT_{\text{CMB}}}{dt} = -\frac{4\pi r_{\text{CMB}}^2 F_{\text{CMB}}}{m_{\text{core}} c_{\text{core}} \hat{T}_{\text{core}}} \quad (9)$$

where m_{core} , c_{core} , \hat{T}_{core} , and F_{CMB} are the mass, heat capacity, thermal structure correction factor of the core, and heat flux at the CMB, respectively (Bower et al. 2018). The core heat capacity c_{core} is prescribed as a constant value representative of liquid iron ($880 \text{ J kg}^{-1} \text{ K}^{-1}$), assuming an isentropic, well-mixed core.

Material properties are computed using separate equations of state for the melt and solid phases. The MgSiO_3 melt is described using the RTpress equation of state (Wolf & Bower 2018), which spans a wide pressure–entropy (P – S) range and is calibrated to experimental data using a limited set of physical parameters. For the solid phase, we adopted the MgSiO_3 equation of state from Mosenfelder et al. (2009). For the mixed-phase region, the properties are computed according to the local melt fraction Eq. (6), and assuming volume additivity when computing the two-phase adiabat (Solomatov 2007). In this case, the melting curves employed are joint data to cover the entire mantle pressure range. At high pressures, the solidus and liquidus are derived from experiments on synthetic chondritic compositions (Andrault et al. 2011), while at lower pressures the melting relations follow the peridotite-based parametrization compiled by Hamano et al. (2013). These datasets are smoothly joined to provide continuous melting curves across the mantle.

2.6. Effect of $f\text{O}_2$ on mantle solidus

Building on the thermodynamic framework provided by the adopted equations of state, we now describe how variations in oxygen fugacity influence mantle melting relations. The melting temperature of the mantle depends sensitively on its composition and thermodynamic state, which are strongly regulated by redox conditions. Laboratory measurements by Lin et al. (2024)

showed a strong dependence of the solidus on $f\text{O}_2^{\text{melt}}$ under oxidizing conditions (IW+2.0) at pressures of 16–26 GPa. Comparing these results with previous experiments under more reducing conditions (Trønnes 2000; Trønnes & Frost 2002; Ishii et al. 2018), they find a shift of several log units in $f\text{O}_2^{\text{melt}}$ between the two regimes. This behaviour can be expressed as:

$$T_{\text{solidus}}^{f\text{O}_2} (\pm 383\text{K}) = T_{\text{solidus}}^{\text{IW}+2.0} + \frac{340}{3.2} \Delta \log f\text{O}_2, \quad (10)$$

With $\Delta \log f\text{O}_2$ being the difference in log units between IW+2.0 (reference solidus) and the target $f\text{O}_2$, and the $\pm 383 \text{ K}$ term reflects the experimental uncertainty on the solidus temperature derived from the Lin et al. (2024) measurements. This would imply that very reducing mantles like the early Earth ($f\text{O}_2 \approx \text{IW}-4.0$) should have a significantly higher melting temperature, whereas more oxidizing conditions lead to a lower melting temperature. This suggests that melting processes, redox evolution, outgassing, atmospheric composition and greenhouse effects form an emergent, coupled system that cannot be treated piecewise in isolation. To investigate these coupled interactions, we applied the Lin et al. (2024) redox-dependent shift (Equation 10) to the baseline melting curves used in our thermo-physical model (Section 2.5).

In this study, the applied offsets produce the expected monotonic trend: reducing conditions (IW–4.0) shift the melting curves to higher temperature, whereas oxidizing conditions (IW+4.0) shift them to lower temperature. Because robust parametrizations describing the redox dependence of the liquidus are currently unavailable due to the limited experimental constraints, we applied the same temperature offset derived for the solidus to the liquidus for each redox state. This preserves the relative separation between solidus and liquidus while shifting the melting interval consistently with redox conditions. The resulting set of redox-dependent melting curves is shown in Fig. 2.

In our framework, these redox-dependent melting curves provide a convenient parametrization of melting behaviour as a function of redox state and are used directly within SPIDER to compute the melt fraction. We noted, however, that oxygen fugacity is fundamentally an outcome of thermodynamic equilibrium rather than an independently imposed parameter. During magma ocean evolution, melting induces phase separation and element partitioning, which can modify the $\text{Fe}^{3+}/\text{Fe}^{2+}$ ratio and hence the effective $f\text{O}_2$, leading to a corresponding evolution of the melting relations themselves. In this work, we therefore adopted a simplified approach in which redox-dependent offsets to the melting curves are prescribed, and should be interpreted as a first-order approximation to this coupled thermochemical behaviour.

Because the oxidation state of the mantle is likely inhomogeneous with pressure, we incorporated two distinct effects of $f\text{O}_2$ that reflect two different physical roles of redox state during magma–atmosphere evolution. In both cases, we explored the same range of redox conditions (IW–4.0, IW–2.0, IW+0, IW+2.0, IW+4.0), allowing us to connect interior melting behaviour with surface outgassing. The individual effects of these two $f\text{O}_2$ terms are detailed as follows:

1. Deep-mantle oxidation state $f\text{O}_2^{\text{melt}}$ controlling the melting curves. $f\text{O}_2^{\text{melt}}$ enters our model through the redox-dependent shift of the melting curves, as described in Section 2.6; we applied the chosen value of $f\text{O}_2$ to adjust the melting curve used by the interior model. This $f\text{O}_2^{\text{melt}}$ value expresses the thermo-physical and compositional state of the interior.

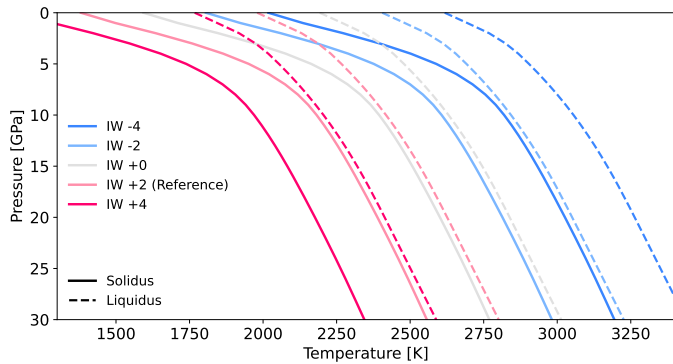


Fig. 2. Solidus (solid lines) and liquidus (dashed lines) for mantle redox states relative to the iron–wüstite buffer (IW-4.0, IW-2.0, IW+0, IW+2.0, IW+4.0). Colours indicate increasing oxidation from dark blue (IW-4.0) to pink (IW+4.0). The reference melting curves correspond to IW+2.0, representing an oxidized, broadly Earth-like mantle state consistent with experimental constraints (Andraut et al. 2011; Hamano et al. 2013). Other curves are obtained by applying the redox-dependent parametrization of Lin et al. (2024). Curves are shown up to 30 GPa for visualisation, although the full melting curves extends to 400 GPa; the redox-dependent temperature offset remains constant across this pressure range.

2. Surface oxidation state fO_2^{surf} governing outgassing and volatile speciation. We parametrized fO_2^{surf} to express the oxidation state at the surface. This value is used in the CALLIOPE module, where it controls volatile speciation and the composition of the outgassed atmosphere. Due to near-surface processes, in particular the pressure dependence of fO_2 , fO_2^{surf} may differ by orders of magnitude from fO_2^{melt} . This behaviour is consistent with Earth, where near-surface reservoirs maintain oxidation states substantially higher than those of the bulk mantle (Cottrell et al. 2025).

Varying fO_2^{surf} and fO_2^{melt} independently enables us to investigate how mantle redox conditions shape atmospheric composition during the magma-ocean stage. By allowing interior and outgassing fO_2 values to vary separately, the model provides a first-order approach for exploring how potential redox gradients between the deep mantle and the magma ocean surface influence thermal and chemical evolution.

2.7. Parameter space exploration

To test the effects of the varying redox states on the geophysical and melting evolution of young rocky planets, we ran a grid of simulations for the specific case of the super-Earth exoplanet GJ 1132 b, where we fixed the melting curve at different redox states to study the possible implications on the subsequent formation of the atmosphere and the evolution of mantle melt fraction. We also explored the orbital distance of exoplanets as exerting significant control over the stellar irradiation, which strongly affects the total heat flux to space. We probed a temperate and highly irradiated case. The orbital separation a was set by defining two reference instillations at 4.5 Gyr for an Earth-like planet, such that our simulated planets receive (i) the stellar irradiation as the Earth today at an age of 4.5 Gyr, and (ii) the same as the real exoplanet GJ 1132 b.

Primordial volatile inventories and bulk compositions of close-in rocky exoplanets remain poorly constrained, motivating an exploration of a wide range of plausible initial conditions. We therefore varied both the initial C/H ratio and the total hy-

Table 1. Overview of the parameter space explored in this study.

Parameter	Values
fO_2^{melt} , relative to IW+2	-4.0, -2.0, 0.0, +2.0, +4.0
fO_2^{surf}	-4.0, -2.0, 0.0, +2.0, +4.0
Total planet mass [M_{\oplus}]	1.0, 3.0
Semimajor axis [au]	0.0153, 0.0700
Bulk inventory [H_{oceans}]	3, 10, 100
Bulk C/H mass ratio	0.1, 2.0

drogen abundance across a broad parameter space in units of Earth oceans. Our nominal values are guided by estimates for the early Earth (Wang et al. 2018), whereas oxygen fugacity is varied across a range motivated by expected mineralogical diversity, which alone may generate differences of at least four log units in fO_2 (Guimond et al. 2023), extending from highly reduced Mercury-like conditions (Cartier & Wood 2019) to more oxidized scenarios like the Earth’s mantle today (Stagno & Fei 2020). In all simulations, we adopted a fixed core radius fraction of $0.55 R_p$ and an initial surface temperature of 3300 K, chosen to ensure that the initial adiabat lies above the liquidus throughout the mantle. This approach allows us to assess the sensitivity of magma ocean evolution and volatile outgassing to poorly constrained initial compositions. The complete simulation grid comprises 600 models and is summarized in Table 1.

3. Results

3.1. Effect of redox-dependent melting curves on thermal evolution

To begin with, we explored how the redox-dependent melting behaviour introduced in Section 2.6 affects the thermal evolution of the planetary interior during magma ocean evolution. Fig. 3 compares two representative simulations with an initial hydrogen inventory of $3 H_{\text{oceans}}$, computed under an instellation equal to Earth’s present-day incident flux, which differ only in their choice of melting curves: the unshifted experimentally based curves from Andraut et al. (2011) and Hamano et al. (2013), and the same curves shifted according to the redox-dependent parametrization of Lin et al. (2024) assuming the mantle is buffered at IW+2.0 relative to the iron–wüstite buffer. As a result of the differing melting curves, the thermal evolution is not a simple rescaling of temperature: shifts in the melting region produce a markedly non-linear response in the coupled interior–atmosphere system.

In the baseline case, a cooler set of melting curves allows a substantial region of the mantle to remain partially molten over an extended period. The melt is relatively well distributed throughout the interior, and the planet cools through a long-lived phase in which deep melt continues to supply heat to the surface. In contrast, the shifted IW-2.0 melting curves favours earlier and more extensive crystallisation at depth. As the rheological front moves upward, melt becomes increasingly confined to a thin shell near the surface, so that the late-time configuration is dominated by a shallow surface magma ocean rather than a deeply distributed molten layer.

In both simulations, we followed the evolution until they reach a steady state, but the internal melt distribution and atmospheric structure differ substantially. In both cases, the thermal profile rapidly approaches the rheological transition, which sets the bulk melt fraction and thereby regulates volatile partitioning between the interior and atmosphere. In our simulations, the

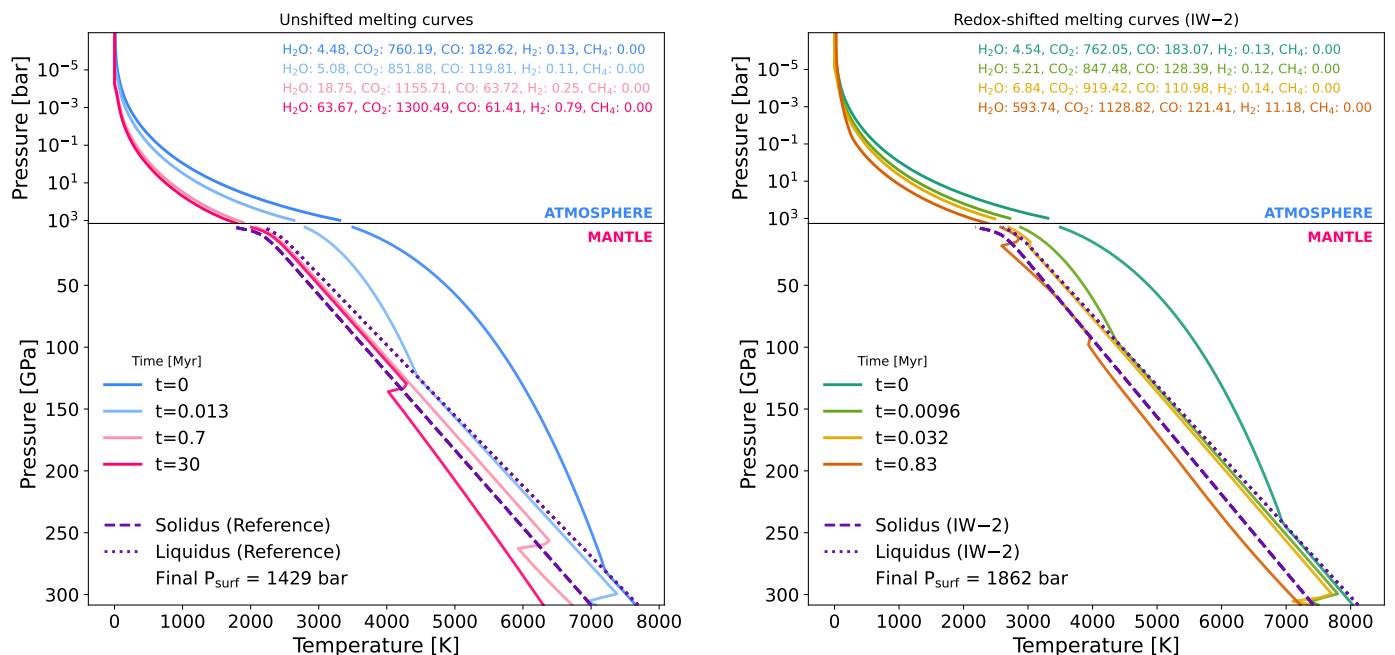


Fig. 3. T - P profiles for two simulations of a $3 M_{\oplus}$ planet showing the coupled interior-atmosphere evolution from an initially global magma ocean to radiative equilibrium (partial pressures in bar). Left: Baseline melting curves from Andraut et al. (2011); Hamano et al. (2013). The mantle remains partially molten for an extended period and solidifies through fractional crystallisation, reaching steady state after ~ 30 Myr with a surface pressure of ≈ 1429 bar. Right: Redox-dependent melting curves shifted to higher temperatures (IW-2.0). Earlier deep-mantle crystallisation confines melt to a shallow magma ocean sustained by greenhouse warming from outgassed water. Steady state is reached after 0.83 Myr with a surface pressure of ≈ 1862 bar.

rheological front marks the depth at which the effective viscosity increases abruptly from $\sim 10^2$ to $\sim 10^{22}$ Pa s, separating low-viscosity convecting melt from a high-viscosity, partially crystallized layer. This transition arises from the viscosity parametrization as a function of melt fraction, with a sharp increase occurring around a critical melt fraction of $\sim 40\%$, where the solid phase starts to control the dynamic timescale (Bower et al. 2022). In the IW-2.0 case, water initially dissolved in the deep magma is progressively exsolved as crystallisation proceeds, increasing the atmospheric opacity and enhancing greenhouse warming. This feedback allows the thin, near-surface magma layer to persist even after most of the deeper mantle has solidified. The comparison demonstrates that an $f\text{O}_2^{\text{melt}}$ -dependent shift of the melting curves does not simply modify the overall thermal state, but instead shifts the reference point relative to the rheological transition. This alters the position of the rheological front and, consequently, the timescales and volatile evolution pathways, determining whether the system evolves toward a deep, partially molten interior or a shallow surface magma ocean.

3.2. Impact of parameters on the interior properties

As a next step, we characterised the diversity of final states and magma ocean lifetimes by examining the global structure of the parameter grid. We analysed a suite of 505 out of 600 simulations that successfully ran to completion, where the 600 models result from the combination of all parameter values listed in Table 1. The remaining 95 simulations did not converge, predominantly at the most reducing melting curve (IW-4.0), where the elevated solidus temperatures led to numerical instabilities at high pressures. All converged simulations reached radiative equilibrium before fully solidifying, indicating the presence of long-lived magma oceans of varying sizes. Regarding the choice

of 200 Myr integration time, as noted in Section 2, the key phases of magma ocean evolution occur within the first tens to hundreds of megayears (Nicholls et al. 2024). The converged simulations all reach radiative equilibrium well within this timescale, suggesting that extending the cutoff further would not significantly affect our results. Fig 4 shows the distribution of interior properties as a function of the main physical and compositional drivers, with rows representing the independent parameters (C/H ratio, surface redox state $\log(f\text{O}_2^{\text{surf}}/\text{IW})$, orbital separation, hydrogen inventory, planet mass, and deep-mantle oxidation state $f\text{O}_2^{\text{melt}}$) and columns corresponding to key outcome variables (solidification time, melt fraction, rheological-front depth, and near-surface surface temperature). The density distributions demonstrate that not all regions of parameter space contribute equally: some parameter combinations cluster around distinct evolutionary pathways, while others produce more extreme or less frequent outcomes.

Two overarching features emerged from these distributions. First, the rheological front depth (Fig.4, third column; panels A3-F3) exhibits a pronounced bi-modality, with peaks near the core-mantle boundary and close to the surface. This bi-modality reflects the existence of two dominant evolutionary pathways (first column; panels A1-F1): planets that reach radiative equilibrium at very early stages while remaining fully molten, characterized by near-unity melt fractions and rheological fronts anchored at the core-mantle boundary (located at ~ 0.55 in normalized planetary radius, corresponding to the adopted core radius fraction), and planets that undergo partial crystallisation near the surface, leading to reduced melt fractions and shallow viscosity contrasts. To complement the density distributions (Fig 4), we additionally showed cumulative distributions (Fig A.1 in Appendix) to quantify the fraction of the simulation ensemble that

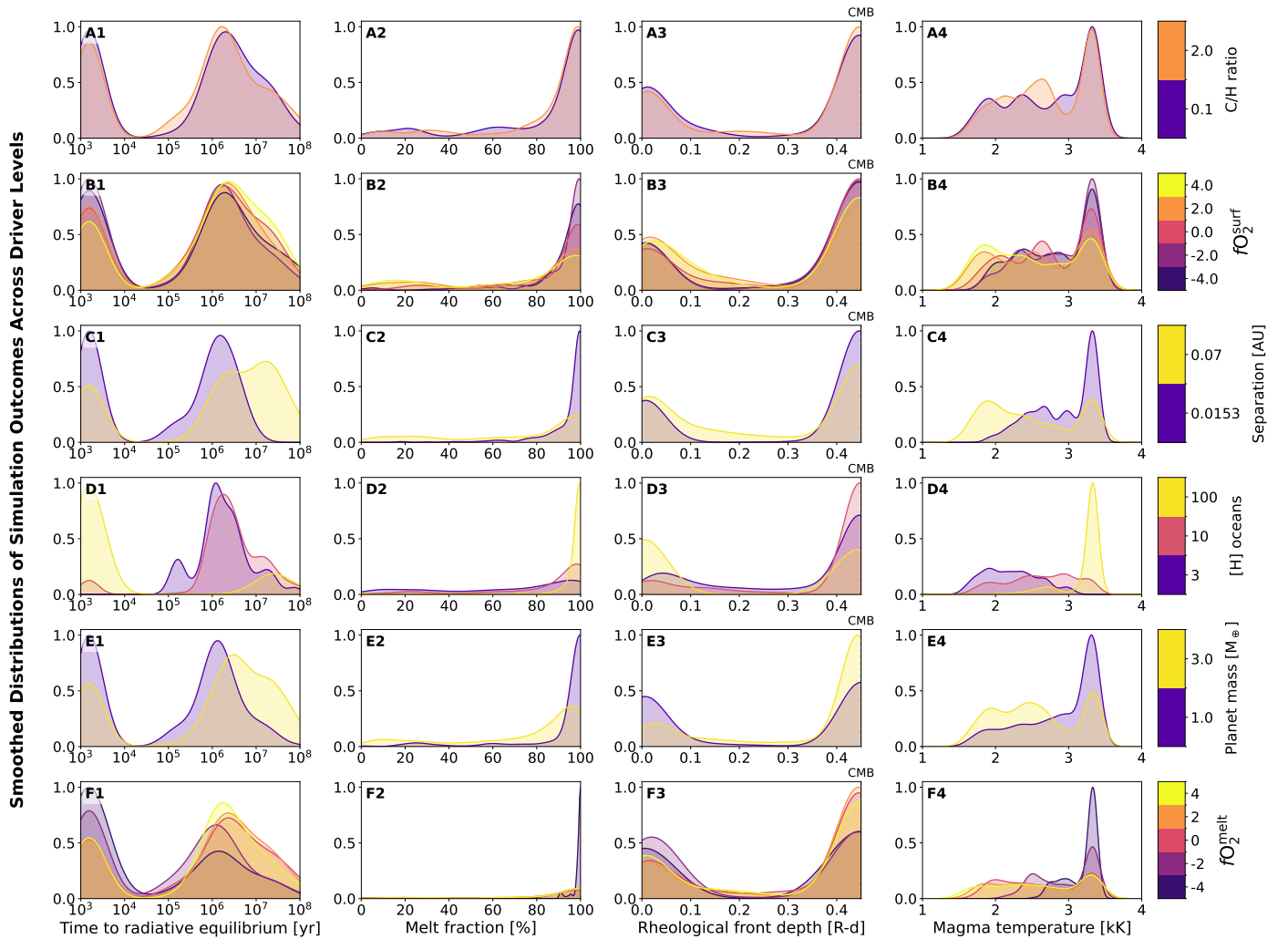


Fig. 4. Smoothed distributions of simulation outcomes across the parameter grid. Rows show variations in the driving parameters (C/H ratio, surface oxidation state fO_2^{surf} relative to the iron–wüstite buffer, orbital separation, volatile inventory in H-ocean mass, planetary mass, and deep-mantle oxidation state fO_2^{melt}), while columns show interior outcomes (time to radiative equilibrium, bulk melt fraction, rheological-front depth, and surface temperature). Coloured curves represent kernel density estimates of simulations sharing a given parameter value. This smoothing is used only for visualisation to highlight trends and clustering across the discrete simulation outcomes.

occupies each regime and to verify that the inferred shifts are systematic rather than driven by low-probability tails.

Among the individual driver parameters, the deep-mantle oxidation state fO_2^{melt} emerges as an important parameter for the melt reservoir through redox-dependent shifts (Fig 4 row F). Reduced melting curves systematically favour earlier interior crystallisation and higher surface temperatures, whereas oxidized melting curves maintain lower melt fractions and delay crystallisation. The surface oxidation state fO_2^{surf} exerts a primary control on surface temperature through its impact on volatile speciation affecting atmospheric composition and the consequent radiative feedbacks, producing modest shifts toward lower temperatures under more oxidized surface conditions (panel B4).

Initial volatile inventories, particularly hydrogen abundance (row D), further regulate surface temperature and melt persistence by controlling greenhouse blanketing and the timing at which radiative equilibrium is established. Large H_{oceans} drive a substantial fraction of simulations toward near 100% melt fractions (panel D2) and higher surface temperatures (panel D4), because volatile-rich planets can reach radiative equilibrium early while remaining fully molten. In this volatile-rich limit, the evo-

lution of the rheological front is therefore primarily set by atmospheric feedbacks. As a consequence, fO_2^{melt} exerts a reduced influence on the evolution, and fO_2^{surf} instead controls both the total atmospheric mass and its speciation. Variations in the C/H ratio further modulate this behaviour (Fig 5 panel A1), as carbon-bearing species exhibit low solubility and preferentially partition into the atmosphere, contributing to the bi modality observed in rheological front regimes.

Structural and orbital parameters introduce additional but subdominant effects (row C). Close-in and low mass planets populate hotter regimes, while more distant and more massive planets preferentially occupy cooler states. These trends mainly redistribute the population along the surface temperature without altering the underlying bimodal structure.

Taken together, the combined density distributions and cumulative statistics demonstrate that magma-ocean evolution is governed by a hierarchy of controls. The volatile inventory acts as the primary regulator, determining whether fO_2^{melt} can modulate the melt reservoir size and consequently the atmospheric feedbacks that set the surface temperature. Orbital separation

and planet mass play subordinate roles within the explored parameter space.

3.3. Impact of parameters on atmospheric properties

Similarly, Fig 5 and A.2 shows the distribution of atmospheric outcomes across the full parameter grid as a function of the main physical and compositional drivers in the PROTEUS simulations. Each column represents a key atmospheric quantity, including total surface pressure, and the H₂O and CO₂ partial pressure. The overlapping probability and cumulative distributions provide a sensitivity map of how different input parameters regulate volatile outgassing and atmospheric composition.

Initially, the bulk C/H ratio distributions primarily reflect the melt state established by volatile-rich cases that reach radiative equilibrium early in their evolution. Within this framework, variations in C/H modulate how carbon is partitioned between the interior and the atmosphere. Because carbon is only weakly soluble in silicate melt, simulations that remain largely molten preferentially retain carbon-bearing species in the atmosphere, leading to enhanced surface pressures in carbon-rich systems. These effects are compounded by carbon's high molecular weight, which further enhances surface pressure in C-dominated atmospheres, consistent with the results shown in Bower et al. (2022).

The surface oxidation state fO_2^{surf} exerts a primary control on regulating atmospheric speciation. Variations in fO_2^{surf} produce important changes in H₂O and CO₂ partial pressures. Orbital separation shows only a weak influence on atmospheric outcomes (row C). While more distant planets tend to occupy slightly cooler regimes, the surface and partial pressures remain broadly similar across the explored range. Therefore, during the magma ocean stage, volatile in/outgassing are primarily controlled by internal thermochemical processes rather than external irradiation, for these two modestly-irradiated scenarios. The initial hydrogen inventory strongly regulates atmospheric mass and thermal state through greenhouse feedbacks. Large volatile budgets (10–100 H_{oceans}) drive a substantial fraction of simulations toward high surface pressures, near-unity melt fractions, and elevated surface temperatures.

Planetary mass (row E) introduces only minor variations in atmospheric outcomes across the explored parameter space. In our model, mass enters the interior structure through hydrostatic equilibrium, where it determines the radial pressure profile and thus the mantle grid, and through the gravitational acceleration (g), which controls the pressure–depth relation and influences volatile solubility and degassing. In the atmosphere, g further affects the pressure structure and radiative properties. Despite these dependencies, the distributions of total atmospheric mass, surface pressure, and volatile partial pressures remain broadly similar for the 1 M_{\oplus} and 3 M_{\oplus} cases, indicating that gravitational and structural effects play a limited role in regulating outgassing in these scenarios.

Finally, the deep-mantle oxidation state fO_2^{melt} (row F) affects atmospheric properties through its control on mantle melt reservoir size as mentioned in Section 3.2, therefore showing higher total surface pressures for reducing fO_2^{melt} , due to early crystallisation and outgassing of volatiles.

3.4. Impact of fO_2^{melt} on atmospheric composition

To examine in more detail how fO_2^{melt} and volatile inventory shape the chemical structure of the outgassed atmospheres, we

next analysed the final surface pressure and volatile speciation as a function of fO_2^{melt} and hydrogen inventory quantified in Earth oceans. While the impactograms in Fig 5 summarize global sensitivities across the parameter space, the following figures resolve individual volatile contributions and quantify how different species partition into the atmosphere under contrasting redox and inventory regimes. This allows us to directly link deep-mantle oxidation state and volatile budgets to observable atmospheric compositions.

Figure 6 shows the median final surface pressure (P_{surf}) and atmospheric composition for simulations with 3, 10, and 100 H_{oceans} . Bars are stacked by volatile species (H₂O, CO₂, CO, H₂, CH₄), illustrating the relative contribution of each gas to the total pressure.

The results reveal a systematic decrease in total surface pressure with increasing deep-mantle oxidation state fO_2^{melt} , consistent across all volatile inventories. Under strongly reducing melting conditions ($fO_2^{\text{melt}} = \text{IW}-4.0$ to $\text{IW}-2.0$), the atmospheres are thick and dominated by H₂ and CO, with pressures reaching 238 bar for 3 H_{oceans} and exceeding 3500 bar for 100 H_{oceans} . As fO_2^{melt} becomes more oxidizing ($\Delta\text{IW} > 0$) along the melting curve, the total pressure drops sharply—by an order of magnitude in the low-volatile cases—while the relative abundance of oxidized species (CO₂ and H₂O) increases. This transition marks a fO_2^{surf} -controlled compositional switch from H₂-rich reducing atmospheres to CO/CO₂-rich oxidizing ones, reflecting equilibrium partitioning during magma ocean outgassing. In parallel, the initial hydrogen inventory also plays a major role: larger volatile budgets (10–100 H_{oceans}) yield proportionally more massive atmospheres, consistent with expectations from equilibrium models (Sossi et al. 2020; Nicholls et al. 2024; Shorttle et al. 2024).

3.5. Impact of fO_2^{melt} on bulk melt fraction

Additionally, Fig 7 further shows that the bulk melt fraction provides a unifying control on volatile partitioning by setting the effective size of the silicate reservoir available for dissolution as mentioned before. In volatile-rich cases ($H_{\text{oceans}}=100$), the mantle remains nearly fully molten and reaches equilibrium rapidly, such that the reservoir size is both large and nearly constant in time. As a result, differences in fO_2^{melt} produce only minor variations in melt fraction and therefore have a negligible impact on volatile partitioning. In contrast, volatile-poor systems ($H_{\text{oceans}}=3$) evolve over longer timescales and exhibit substantial changes in melt fraction, reflecting a progressively shrinking reservoir. Consequently, variations in fO_2^{melt} strongly affect the rate and extent of crystallization, and therefore directly control the mass of volatiles that can be retained in the interior versus released to the atmosphere. This behaviour is consistent with the trends identified in the impactogram A.1, and supports a simplified interpretation in which deep-mantle redox state governs the mass balance of volatile partitioning through its control on bulk melt fraction, while surface redox conditions regulate the chemical speciation of the atmosphere.

Overall, these results demonstrate that the deep-mantle oxidation state fO_2^{melt} and the initial volatile inventory jointly regulate the timing and the amount of volatiles released by controlling how the bulk melt fraction evolves over time. As the interior progressively solidifies, volatiles are released at different rates, while the surface temperature further influences atmospheric composition and, in turn, the cooling rate. By controlling the mantle melting curves and therefore the melt fraction, fO_2^{melt} governs how long and how extensively the man-

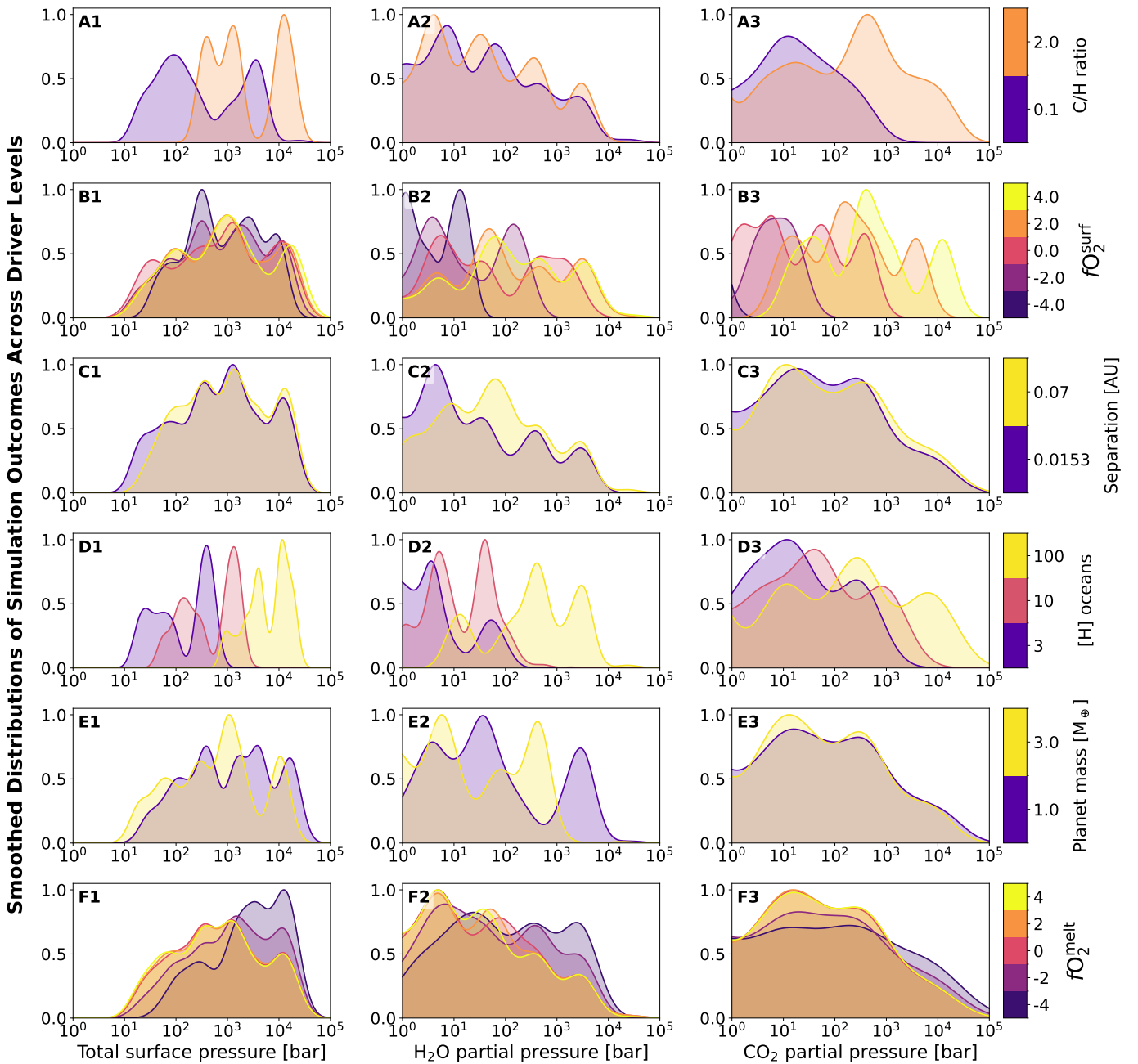


Fig. 5. Smoothed density distributions of atmospheric outcomes across the parameter grid. Rows show variations in the driving parameters (C/H ratio, surface oxidation state fO_2^{surf} relative to the iron–wüstite buffer, orbital separation, volatile inventory in H-ocean mass, planetary mass, and deep-mantle oxidation state fO_2^{melt}), while columns show interior outcomes (time to radiative equilibrium, bulk melt fraction, rheological-front depth, and surface temperature). Coloured curves represent kernel density estimates of simulations sharing a given parameter value. This smoothing is used only for visualisation to highlight trends and clustering across the discrete simulation outcomes.

tle remains molten, which in turn determines the capacity of the interior to exchange volatiles with the atmosphere. In contrast, the surface oxidation state fO_2^{surf} primarily controls atmospheric speciation by regulating near-surface chemical equilibria, determining whether outgassed volatiles are retained as H_2 -rich or CO_2 -dominated atmospheres. While higher water inventories mainly set the absolute atmospheric mass by sustaining large and persistent magma oceans, they do not systematically follow the redox-dependent melting trends imposed by fO_2^{melt} . Together with the distribution analysis in Fig 6, these results show that the combined effects of deep-mantle melting behaviour and surface redox chemistry control the distribution

of atmospheric outcomes—from thick, H_2 -rich atmospheres to thinner, oxidized envelopes—across different redox states, primarily in volatile-poor systems. This coupling implies that the final atmospheric composition, and more indirectly the surface pressure, may retain signatures of the planet’s interior oxidation state, with observable molecular abundances providing the most robust diagnostic.

3.6. Impact of fO_2^{melt} on interior-atmosphere partitioning

Finally, Fig 8 summarizes the atmosphere-interior partitioning of major volatile species as a function of deep-mantle oxida-

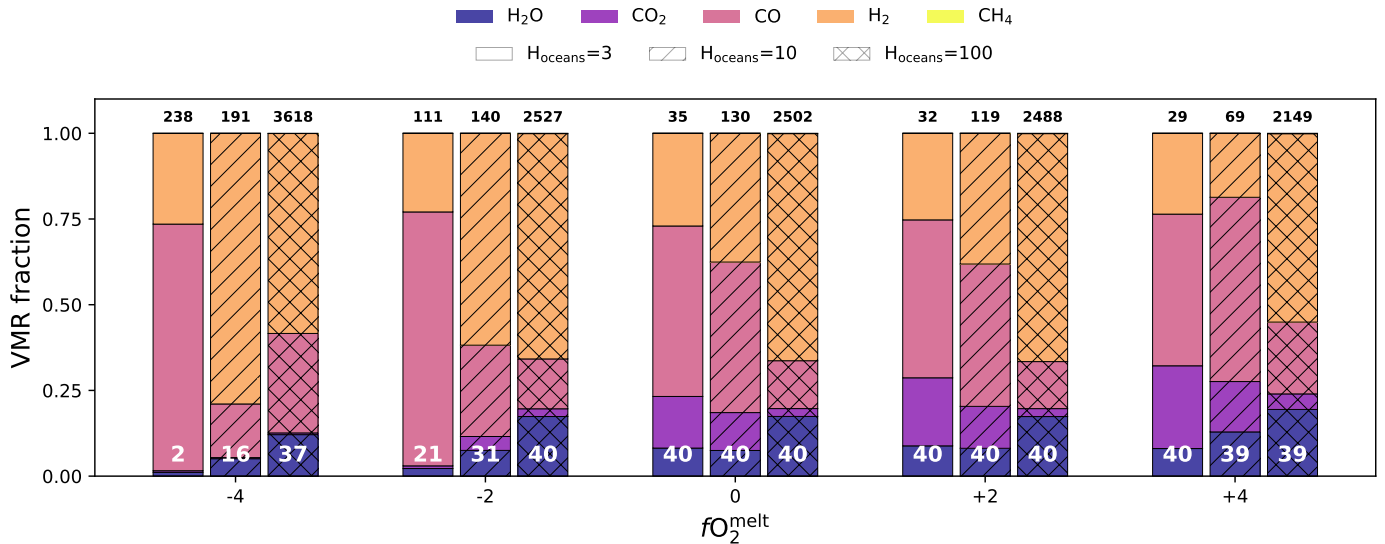


Fig. 6. Volume mixing ratio of outgassed volatiles as a function of the deep-mantle oxidation state fO_2^{melt} for simulations with initial water inventories of 3, 10, and 100 H_{oceans} . Numbers within the bars indicate the number of simulations contributing to each median value and numbers on top of each bar represent the median surface pressure P_{surf} in bar. Colours denote the relative contributions of major atmospheric species (H_2O , CO_2 , CO , H_2 , CH_4), while hatch patterns distinguish different volatile inventories. CH_4 is present in individual simulations but contributes negligibly to the median volume mixing ratio and is therefore not visible in the stacked bars. The low number of converged simulations for $H_{\text{oceans}} = 3$ at $fO_2^{\text{melt}} = IW - 4$ ($n = 2$) reflects numerical instabilities arising from the elevated solidus temperatures under strongly reducing conditions, which prevented convergence in most of these runs.

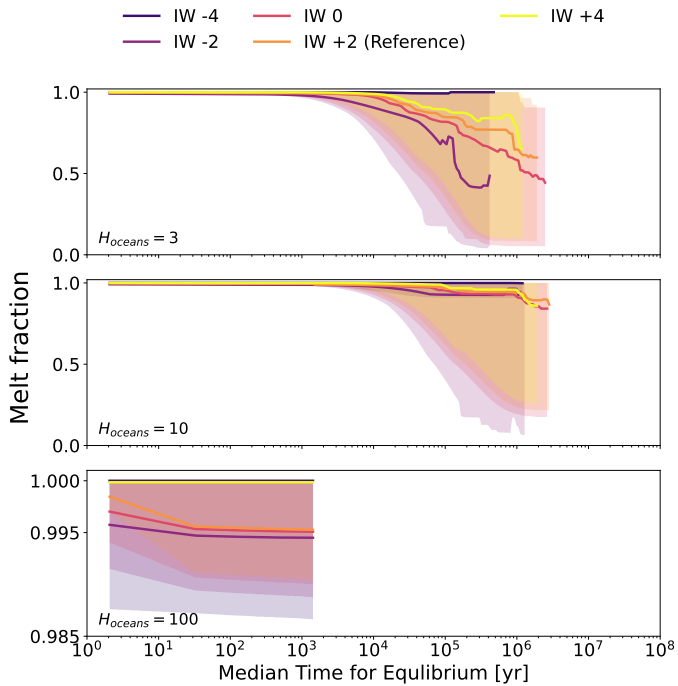


Fig. 7. Evolution of the mantle melt fraction with time for three initial water inventories ($H_{\text{oceans}} = 3, 10, 100$; top to bottom) and different redox-dependent melting scenarios (fO_2^{melt} : IW-4.0 to IW+4.0). Curves show the median across simulations at each time, with shaded regions indicating the full range. Each curve is truncated at the median time for equilibrium.

tion state fO_2^{melt} and initial volatile inventory. Each panel corresponds to simulations with 3, 10, and 100 H_{oceans} , and colours indicate the median logarithmic ratio of atmospheric to interior volatile mass, $\log M_{\text{atm}}/M_{\text{int}}$, for each species and fO_2^{melt} . Posi-

tive values denote atmosphere-dominated partitioning, whereas negative values indicate preferential retention within the mantle. This representation provides a direct, quantitative measure of degassing efficiency and reveals how mantle redox conditions and volatile inventory jointly regulate volatile partitioning during magma ocean outgassing.

Across all simulations, H_2O remains strongly retained within the mantle, with median values of $\log M_{\text{atm}}/M_{\text{int}} \approx -2$ to -1 , indicating that only a few percent of the total H_2O inventory is transferred to the atmosphere. This behaviour reflects the high solubility of water in silicate melt and its limited degassing efficiency under high melt fractions (Bower et al. 2022, 2025). In contrast, carbon-bearing species exhibit a pronounced behaviour with fO_2^{melt} . Both CO and CO_2 preferentially partition into the atmosphere, with typical ratios of $\log M_{\text{atm}}/M_{\text{int}} \approx +1.5$ to $+0.8$ under reducing conditions. CO_2 displays its highest atmosphere-interior ratios in reduced mantles and progressively lower values toward more oxidizing regimes, reflecting the redox-dependent melting behaviour imposed by fO_2^{melt} , with enhanced interior retention at high oxidation states due to high melt fractions.

Hydrogen-bearing species show the strongest partitioning contrast. Molecular hydrogen is highly atmosphere-dominated across all redox states, with $\log M_{\text{atm}}/M_{\text{int}} \approx 48$ – 52 . These extreme values arise specifically for H_2 , which is effectively insoluble in silicate melt and therefore absent from the interior (Sossi et al. 2023); for visualisation facilities, interior H_2 masses are represented using a minimum value of 10^{-30} kg. Methane also preferentially partitions into the atmosphere, but exhibits a fO_2^{melt} -dependent behaviour similar to that of carbon-bearing species, with higher $\log M_{\text{atm}}/M_{\text{int}}$ ratios under reducing conditions and progressively lower values toward oxidizing regimes.

Comparison across volatile inventories indicates that volatile-poor systems often display more extreme $\log M_{\text{atm}}/M_{\text{int}}$ ratios, implying stronger preferential partitioning into either the atmosphere or the interior. In contrast, volatile-rich cases generally exhibit smaller ratios for the same species and redox con-

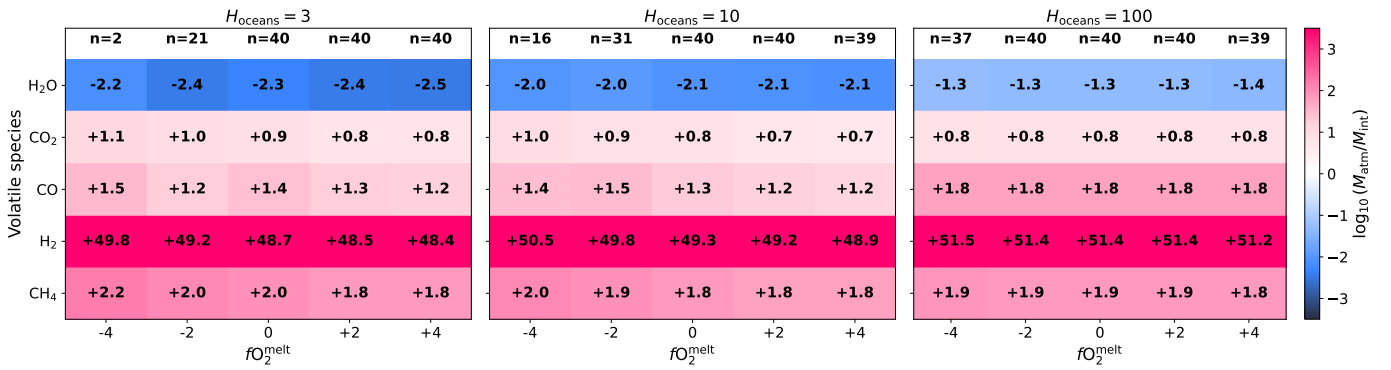


Fig. 8. Atmosphere-interior partitioning of major volatile species as a function of deep-mantle oxidation state fO_2^{melt} and initial volatile inventory. Each panel corresponds to a different initial H inventory (3, 10, and 100 H_{oceans}). Colours indicate the median logarithmic ratio of atmospheric to interior volatile mass, $\log M_{\text{atm}}/M_{\text{int}}$, for each species and oxidation state offset along the melting curve (fO_2^{melt} , expressed relative to the IW+2.0). Positive values denote atmosphere-dominated partitioning, whereas negative values indicate retention within the mantle. Numbers above each column indicate the number of converged simulations contributing to each bin. The figure highlights three distinct regimes: persistent interior buffering of H₂O, systematic atmospheric dominance of H₂, and strong redox-dependent partitioning of carbon-bearing species.

ditions, reflecting a more balanced distribution of volatiles between the mantle and the atmosphere. Overall, these results show that volatile partitioning is primarily controlled by the bulk melt fraction, which governs the efficiency of degassing. The melt fraction is, in turn, modulated by the deep-mantle oxidation state fO_2^{melt} through its influence on the melting curves. As a result, the impact of fO_2^{melt} on volatile partitioning is indirect and most pronounced in volatile-poor systems, whereas the initial volatile inventory mainly sets the absolute atmospheric mass. The chemical speciation of the outgassed volatiles is determined by near-surface conditions during degassing (Gaillard & Scaillet 2014), rather than by deep-mantle redox alone.

4. Discussion

A central question of this study is whether the fO_2^{melt} -dependent melting temperature differences can meaningfully influence planetary evolution. Our results show that the answer depends critically on the volatile inventory. Redox state undoubtedly affects the melting curve: reducing conditions shift it to higher temperatures, whereas oxidizing conditions lower it. This offset determines when the temperature profile first intersects the solidus and, consequently, the conditions under which solidification initiates. However, whether this difference propagates into large-scale evolutionary consequences depends on whether the thermal profile intersects the melting curves before the system approaches thermal equilibrium.

In volatile-rich cases ($H_{\text{oceans}} = 10\text{--}100$), the mantle thermal profile remains far above the solidus for most of the evolution. These simulations never reach the melting region at all, because the surface cools into radiative equilibrium long before the interior thermal profile approaches the melting point. As a result, even a several-hundred-Kelvin redox shift produces little effect on melt fraction, cooling timescales, or the depth of the convecting layer. In this regime, fO_2^{melt} does not strongly influence the planet's thermal pathway. Instead, the fO_2^{surf} mainly controls the chemistry of the atmosphere: reduced mantles yield H₂–CO-rich envelopes, whereas oxidized mantles favour CO₂–H₂O atmospheres. Differences in final atmospheric mass remain detectable across redox states, but they are not as large as in the volatile-poor case.

By contrast, in volatile-poor cases ($H_{\text{oceans}} = 3$), the interior thermal profile approaches and in some simulations intersects

the melting region before the system reaches radiative equilibrium. Here, fO_2^{melt} plays a decisive role. Hotter melting curves associated with reduced conditions (IW-2.0) shift the melting region to higher temperatures, leading to earlier progression towards solidification at depth and reorganizing the distribution of melt within the planet. Instead of sustaining a deep magma ocean as in the reference case, reduced melting curves promote more extensive interior solidification, reducing the depth of the molten region and confining melt to a shallow near-surface layer. At early times, however, the migration of the rheological front is controlled by the atmospheric cooling rate, as the interior efficiently resupplies heat to the surface. In this configuration, water released during interior solidification increases atmospheric opacity and enhances greenhouse warming, thereby slowing cooling and allowing the shallow surface magma layer to persist. In contrast, cooler melting curves associated with oxidized conditions (IW+2.0 to IW+4.0) allow extensive melting to persist in the deep interior for longer, maintaining a deep and vertically extended magma ocean.

In this volatile-poor regime, therefore, fO_2^{melt} influences not only the timing of crystallisation but also the depth of the magma ocean, the distribution of melt available to host volatiles, and the efficiency of outgassing. These effects amplify differences in atmospheric pressure and composition across redox states, demonstrating that fO_2^{melt} influences both the structure of the mantle and the eventual atmospheric properties for this specific scenario.

4.1. Implications for atmospheric composition and observability

Across the full grid, reduced mantles (IW-4.0 to IW-2.0) produce H₂-dominated atmospheres, with CO as the main carbon carrier. Oxidized mantles (IW+2.0 to IW+4.0) generate CO₂, CO and H₂O-rich envelopes. This reflects well-known fO_2^{surf} -control on volatile speciation: hydrogen and carbon remain volatile under reducing conditions, but oxidize into less volatile species that dissolve more readily in the melt (Sossi et al. 2020; Nicholls et al. 2024; Bower et al. 2025; Lichtenberg et al. 2025).

These compositional trends directly affect the atmospheric mean molecular weight and total surface pressure. Reduced cases generate the most massive atmospheres, often exceeding one kilobar for the volatile-rich cases, while oxidized cases gen-

erate lower-pressure but higher mean molecular weight (MMW) envelopes. The radiative consequences are notable: high pressure H_2+CO atmospheres efficiently trap heat within the planet, through collision-induced absorption (Borysow 2002), potentially prolonging magma ocean lifetimes (Nicholls et al. 2024; Krissansen-Totton et al. 2024). Oxidized atmospheres, though IR-active, are less massive and offer a weaker blanketing effect at late times.

This redox–volatility coupling offers a possible explanation for the atmospheric diversity now being revealed in close-in rocky planets around M dwarfs. Observations of 55 Cnc e (Hu et al. 2024) and TOI-561 b (Teske et al. 2025), for example, indicate volatile-rich envelopes dominated by CO and CO_2 , broadly consistent with the oxidized to moderately reduced regimes identified here. However, other ultra-short period exoplanets do not exhibit signs of an atmosphere (Lichtenberg & Miguel 2025). The high surface pressures and mixed C–O chemistry of the scenarios inferred for these systems could reflect planets that partially solidified from initially reducing magma oceans and later oxidized through volatile loss or mantle crystallisation. Water storage in oxidized mantles has been predicted to affect the long-term bulk volatile composition of observed super-Earths (Dorn & Lichtenberg 2021). Conversely, more reduced cases in our grid predict thick H_2+CO atmospheres. Therefore, our simulations illustrate that redox trends inherited from accretion can affect the distribution of melting in the deep interior, and, by extension, the storage capacity of the mantle over Gyr timescales.

4.2. Benchmarking case

GJ 1132 b provides a particularly valuable benchmark for testing coupled interior–atmosphere evolution models, given the availability of high-precision observational constraints. Early ground-based transmission spectroscopy observations (Diamond-Lowe et al. 2018) already indicated a largely featureless spectrum, disfavoured H_2 -rich atmospheres and suggesting either a high mean molecular weight atmosphere or absence of an atmosphere. Similarly, recent JWST/NIRSpec transmission spectroscopy observations shows that the planet spectrum is best described by a flat continuum (Bennett et al. 2025), consistent with either a very thin steam atmosphere or an atmosphere-free surface. Nevertheless, when combined with MIRI/LRS thermal emission measurements, these data favour the presence of a very thin atmosphere explained by a nearly bare rocky planet (Xue et al. 2024). In this way, forward modelling of the dayside emission spectrum rules out Earth-like atmospheres ($P \sim 1$ bar) containing even modest amounts of H_2O , excludes atmospheres of any thickness (10^{-4} – 10^2 bar) with $\geq 1\%$ CO_2 , and disfavours thick, Venus-like envelopes ($P \geq 100$ bar) with trace amounts of CO_2 or H_2O , indicating that GJ 1132 b most likely lacks a significant volatile atmosphere (Xue et al. 2024).

Within the context of our simulations, the apparent lack of a substantial atmosphere on GJ 1132 b is most consistent with volatile-poor initial conditions and an oxidized deep-mantle state $f\text{O}_2^{\text{melt}}$ that limits sustained melt fractions and long-term volatile release. Reduced and volatile-rich evolutionary pathways in our models tend to produce thick H_2 - and CO-rich atmospheres during early magma-ocean phases, which, although potentially short-lived due to escape, would be expected to leave behind more substantial secondary atmospheres. This interpretation is consistent with the evolutionary models of Schaefer et al. (2016), who investigated the coupled magma ocean–atmosphere evolution of GJ 1132 b. They find that retaining a substantial water-rich atmosphere requires extreme initial volatile invento-

ries ≥ 5 wt% (percent by weight) of H_2O , while most evolutionary pathways lead to tenuous atmospheres. In their models, photodissociation of water and preferential hydrogen escape result in the build-up of abiotic O_2 , with the magma ocean acting as only a limited oxygen sink. As a consequence, the most common outcome is a thin, O_2 -dominated atmosphere, unless a long-lived magma ocean or unusually high initial water content is maintained. The observational evidence for GJ 1132 b therefore favours an evolutionary history in which efficient early atmospheric loss and limited late-stage outgassing suppress the persistence of a detectable present-day atmosphere. Future detections of even weak CO_2 - or H_2O -dominated envelopes would provide valuable constraints on the planet’s initial volatile inventory and redox state, highlighting the potential of GJ 1132 b as a probe of coupled interior–atmosphere evolution (Nicholls et al. 2025b). A key question emerging from our results is whether the interior oxidation state can be constrained from atmospheric observations alone. As shown in Fig 6, volatile inventory exerts a stronger control on total atmospheric mass but not on composition than redox state, while $f\text{O}_2^{\text{surf}}$ primarily controls atmospheric speciation. This introduces a degeneracy between volatile content and oxidation state that is difficult to break from bulk atmospheric properties alone. In this context, accurate atmospheric modelling plays an important role in linking observable upper-atmosphere compositions to near-surface redox chemistry. Mixing processes and photochemical reactions can modify the vertical distribution of molecular species, potentially obscuring or preserving the redox signature of outgassed volatiles in the observable atmosphere (Pierrehumbert 2010). Turbulent mixing and photochemical reactions can modify the vertical distribution of molecular species, potentially obscuring or preserving the redox signature of outgassed volatiles in the observable atmosphere (Shorttle et al. 2024; Nicholls et al. 2025a). While thermochemical equilibrium signatures set in the deep atmosphere may be propagated to observable pressure levels if mixing timescales are short compared to reaction timescales (Tsai et al. 2023; Nicholls et al. 2025a). It should thus be tested under which conditions disequilibrium atmospheric processes could obscure the outgassed volatile composition and thus redox state. Together, these considerations suggest that these kind of modelling, would represent a promising avenue for constraining deep-mantle redox conditions from upcoming JWST and ELT observations. In this study, we assumed volatile exchange only between the melt and atmosphere. In reality, incorporation of H, C, or O through melt trapping or crystal inclusions (Sim et al. 2024; Krissansen-Totton et al. 2024) could increase the total outgassing efficiency and accelerate mantle oxidation, potentially yielding thinner atmospheres and shorter magma ocean lifetimes (Lebrun et al. 2013; Salvador et al. 2017; Nikolaou et al. 2019; Bower et al. 2019). In these cases, melt redistribution due to the effects described here would amplify the ability of the mantle to store or release volatiles (Hier-Majumder & Hirschmann 2017; Sim et al. 2024). The feedbacks between these mechanisms should be studied, but are outside the scope of this work.

Furthermore, atmospheric escape processes are not included. In particular, close-in rocky planets are expected to experience efficient hydrodynamic and energy-limited escape of light species driven by stellar X-ray and extreme ultraviolet irradiation (e.g., Watson et al. (1981); Zahnle & Kasting (1986); Schaefer et al. (2016); Owen (2019)). As a consequence, the large H_2 abundances predicted under reducing conditions in our simulations likely represent upper limits on the long-term atmospheric hydrogen content (Schaefer et al. 2016; Nicholls et al. 2024). However, by varying the initial hydrogen inventory across our

model grid, we effectively explored a range of outcomes that may arise from different escape histories, providing a first-order sensitivity analysis of how atmospheric mass and composition respond to hydrogen loss. In reality, substantial hydrogen loss may occur on relatively short timescales, potentially reducing the persistence and observability of H_2 -rich atmospheres (Schaefer et al. 2016). In particular, predictions concerning the absolute abundance, lifetime, and detectability of H_2 -dominated atmospheres would benefit most from a self-consistent treatment of escape processes.

In addition, we do not explicitly resolve a depth-dependent oxygen fugacity structure. In the present formulation, the redox dependence of melting is implemented as a temperature shift relative to a reference solidus, such that variations in fO_2^{melt} produce a uniform offset while preserving the underlying pressure dependence of the melting curves. As a result, the adopted parametrisation captures first-order redox effects as a global shift in melting behaviour. If fO_2^{melt} were instead resolved as a function of depth, this would lead to local modifications of the solidus temperature at each pressure level, effectively producing a depth-dependent perturbation to the melting relations and potentially shifting the depth at which the interior adiabat intersects the solidus. Near-surface reservoirs are generally expected to be more oxidized than the deep interior. While our parameter grid explores all combinations as a broad sensitivity study, scenarios in which fO_2^{surf} exceeds fO_2^{melt} are the more geophysically realistic ones. Given the complexity of self-consistently coupling a depth-dependent redox profile to the melting parametrisation, we adopted a qualitative approach and treat fO_2^{melt} and fO_2^{surf} as independent parameters, allowing us to bracket the range of plausible interior-atmosphere redox configurations.

Beyond the effects of oxygen fugacity on the melting curves, dissolved water in the melt would further modify our results through two main mechanisms. First, as referenced in Section 1 and Section 2.6 of this study, water depresses the solidus through hydroxylation of the silicate network (Katz et al. 2003), whereby H_2O is incorporated into the melt as OH^- , weakening mineral bonds and stabilizing the liquid phase, with volatile-saturated silicates exhibiting solidus depressions of up to 600–800 K (Dasgupta & Hirschmann 2007; Myhill et al. 2017; Xie et al. 2024). This would tend to maintain higher melt fractions for longer, extending magma ocean lifetimes and affecting outgassing rates, particularly in the volatile-poor regime where the thermal profile approaches the solidus. Second, and not accounted for in our model, water significantly lowers melt viscosity, which would enhance convective heat transport through the mantle. In this way, a less viscous melt would increase the efficiency of convection, therefore accelerating cooling.

Despite these assumptions, the physical trends identified in this work remain robust. Reduced planets may present favourable observational signatures. For low to intermediate volatile inventories ($H_{\text{oceans}} = 10$) and moderately reducing mantles ($IW = 3$ to -2), the resulting H_2 - and CO -rich atmospheres produce strong molecular absorption features in the 3–5 μm range accessible to JWST and future ELT instruments (Katyal et al. 2020; Nicholls et al. 2024). More extremely reduced and volatile-rich cases ($IW \lesssim -4$, $H_{\text{oceans}} = 100$) instead generate very thick H_2 envelopes that may be susceptible to atmospheric escape. In contrast, oxidized mantles produce H_2O - and CO , CO_2 -dominated atmospheres. These compositional differences suggest that future observations may help constrain deep-interior redox states and volatile inventories through atmospheric spectra. Therefore, the initial volatile inventory emerges as the primary control on atmospheric mass, fO_2^{surf} on the volatile spe-

ciation, while the influence of the deep-mantle oxidation state fO_2^{melt} plays a secondary role that depends strongly on the available volatile budget. As recent JWST observations highlight, the atmospheric properties of close-in rocky exoplanets are not yet fully explained. Integrating interior redox evolution, volatile partitioning, water-dependent melting feedbacks and atmospheric escape will therefore be essential for interpreting upcoming detections of secondary atmospheres and for linking observable spectra to the geochemical state of rocky exoplanet interiors like in the case of GJ 1132 b, TOI-561 b, and TOI-6255 b.

5. Conclusions

We upgraded the coupled numerical framework PROTEUS to investigate how deep-mantle redox state (fO_2^{melt}) and volatile inventory jointly shape magma ocean evolution and atmospheric composition in rocky exoplanets, using GJ 1132 b as a reference case. Our approach incorporates fO_2 -dependent shifts in mantle melting curves, allowing us to assess how variations in redox state propagate into the thermal structure, melt fraction, and atmospheric composition. We explored a wide range of redox states ($IW-4.0$ to $IW+4.0$) and volatile inventories to determine under which conditions redox-dependent melting curves significantly influence interior evolution and potentially observable atmospheric properties.

Our results reveal a hierarchy of controls on magma ocean evolution, where volatile inventory sets a primary control on whether the redox-dependent melting relations modulate or not bulk melt fraction, and consequently the size of the melt reservoir available for volatile dissolution and outgassing. Our main conclusions are as follows:

- Redox-dependent shifts in the melting curves become important for volatile-poor planets where the mantle thermal profile approaches the solidus. In this regime, hotter melting curves associated with reducing mantle conditions trigger earlier crystallisation, promote a shallow-surface magma ocean and enhance interior–atmosphere partitioning, whereas cooler melting curves associated with oxidizing conditions prolong the fully molten state and promote a more radially distributed melt reservoir. In contrast, for volatile-rich planets, the mantle thermal profile remains far above the melting region and reaches radiative equilibrium before crystallisation occurs, making the thermal evolution in this regime largely insensitive to fO_2^{melt} .
- While fO_2^{melt} modulates bulk melt fraction in the volatile-poor regime, the surface oxidation state fO_2^{surf} regulates near-surface chemical equilibria and determines the speciation of outgassed volatiles. Reduced surface conditions favour H_2+CO -rich atmospheres, whereas oxidized conditions produce H_2O+CO_2 dominated envelopes.
- Orbital separation plays a secondary role compared to volatile inventory and redox state. Within the parameter space explored for GJ 1132 b, variations in orbital distance produce relatively minor changes in atmospheric outcomes compared with those driven by volatile content or IW .

Future extensions of this work will incorporate time-dependent redox evolution, solid-phase volatile trapping, and atmospheric escape to enable fully self-consistent predictions of thermal evolution and spectroscopic observables for rocky exoplanets.

Acknowledgements. The authors thank the anonymous referee for their constructive comments, which helped improve the manuscript. MS thanks Laura

Kreidberg, Mara Attia, Rob Spaargaren and Christopher Boettner for useful comments and suggestions. This work was partially supported by the Branco Weiss Foundation, the Netherlands eScience Center (PROTEUS project, NLESC.OEC.2023.017), the Alfred P. Sloan Foundation (AETHeR project, G202114194), NASA's Nexus for Exoplanet System Science research coordination network (Alien Earths project, 80NSSC21K0593), and the NWO NWO-ORC PRELIFE Consortium (PRELIFE project, NWA.1630.23.013). HN acknowledges support from STFC grant UKR11184. We also thank the Center for Information Technology of the University of Groningen for their support and for providing access to the Habrok high performance computing cluster.

References

- Abe, Y. 1995, *The Earth's Central Part: Its Structure and Dynamics* (Terra Scientifica)
- Abe, Y. & Matsui, T. 1985, *Lunar and Planetary Science Conference Proceedings*, 90, C545
- Abe, Y. & Matsui, T. 1988, *Journal of the Atmospheric Sciences*, 45, 3081
- Amundsen, D. S., Mayne, N. J., Baraffe, I., et al. 2016, *A&A*, 595, A36
- Andraut, D., Bolfan-Casanova, N., Nigro, G. L., et al. 2011, *Earth and Planetary Science Letters*, 304, 251
- Armstrong, K., Frost, D. J., McCammon, C. A., Rubie, D. C., & Boffa Ballaran, T. 2019, *Science*, 365, 903
- Armstrong, L. S., Hirschmann, M. M., Stanley, B. D., Falksen, E. G., & Jacobsen, S. D. 2015, *Geochim. Cosmochim. Acta*, 171, 283
- Badro, J., Brodholt, J. P., Piet, H., Siebert, J., & Ryerson, F. J. 2015, *Proceedings of the National Academy of Science*, 112, 12310
- Barth, P., Carone, L., Barnes, R., et al. 2021, *Astrobiology*, 21, 1325
- Batygin, K. & Morbidelli, A. 2023, *Formation of rocky super-earths from a narrow ring of planetesimals*
- Bennett, K. A., MacDonald, R. J., Peacock, S., et al. 2025, *AJ*, 170, 205
- Berta-Thompson, Z. K., Irwin, J., Charbonneau, D., et al. 2015, *Nature*, 527, 204
- Boer, I. D., Nicholls, H., & Lichtenberg, T. 2025, *ApJ*, 987, 172
- Borysow, A. 2002, *A&A*, 390, 779
- Boukaré, C.-E., Parmentier, E. M., & Parman, S. W. 2018, *Earth and Planetary Science Letters*, 491, 216
- Boukaré, C.-E., Ricard, Y., & Fiquet, G. 2015, *Journal of Geophysical Research (Solid Earth)*, 120, 6085
- Boukaré, C.-É., Schaefer, L. K., & Rizo, H. 2025, *Physics of the Earth and Planetary Interiors*, 369, 107463
- Bower, D. J., Hakim, K., Sossi, P. A., & Sanan, P. 2022, *The Planetary Science Journal*, 3, 93
- Bower, D. J., Kitzmann, D., Wolf, A. S., et al. 2019, *A&A*, 631, A103
- Bower, D. J., Sanan, P., & Wolf, A. S. 2018, *Physics of the Earth and Planetary Interiors*, 274, 49
- Bower, D. J., Thompson, M. A., Hakim, K., Tian, M., & Sossi, P. A. 2025, *ApJ*, 995, 59
- Canil, D. & O'Neill, H. S. C. 1996, *Journal of Petrology*, 37, 609
- Cartier, C. & Wood, B. J. 2019, *Elements*, 15, 39
- Chase, M. W. 1996, *Journal of Physical and Chemical Reference Data*, 25, 1069
- Cottrell, E., Canil, D., Langmuir, C., Evans, K. A., & Gaillard, F. 2025, *Nature Reviews Earth and Environment*, 6, 728
- Dasgupta, R. & Hirschmann, M. M. 2007, *American Mineralogist*, 92, 370
- Deng, J., Du, Z., Karki, B. B., Ghosh, D. B., & Lee, K. K. M. 2020, *Nature Communications*, 11, 2007
- Diamond-Lowe, H., Berta-Thompson, Z., Charbonneau, D., & Kempton, E. M.-R. 2018, *AJ*, 156, 42
- Dorn, C. & Lichtenberg, T. 2021, *ApJ*, 922, L4
- Edwards, J. M. & Slingo, A. 1996, *Quarterly Journal of the Royal Meteorological Society*, 122, 689
- Elkins-Tanton, L. T. 2008, *Earth and Planetary Science Letters*, 271, 181
- Elkins-Tanton, L. T. 2012, *Annual Review of Earth and Planetary Sciences*, 40, 113
- Elkins-Tanton, L. T., Parmentier, E. M., & Hess, P. C. 2003, *Meteoritics & Planetary Science*, 38, 1753
- Frost, D. J. & McCammon, C. A. 2008, *Annual Review of Earth and Planetary Sciences*, 36, 389
- Gaillard, F., Bernadou, F., Roskosz, M., et al. 2022, *Earth and Planetary Science Letters*, 577, 117255
- Gaillard, F. & Scaillet, B. 2014, *Earth and Planetary Science Letters*, 403, 307
- Gallet, F. & Bouvier, J. 2013, *A&A*, 556, A36
- Gordon, I. E., Rothman, L. S., Hargreaves, R. J., et al. 2022, *J. Quant. Spectr. Rad. Transf.*, 277, 107949
- Grimm, S. L. & Heng, K. 2015, *ApJ*, 808, 182
- Grimm, S. L., Malik, M., Kitzmann, D., et al. 2021, *ApJS*, 253, 30
- Guimond, C. M., Shorttle, O., Jordan, S., & Rudge, J. F. 2023, *MNRAS*, 525, 3703
- Hamano, K., Abe, Y., & Genda, H. 2013, *Nature*, 497, 607
- Hamano, K., Kawahara, H., Abe, Y., Onishi, M., & Hashimoto, G. L. 2015, *ApJ*, 806, 216
- Hier-Majumder, S. & Hirschmann, M. M. 2017, *Geochemistry, Geophysics, Geosystems*, 18, 3078
- Hirschmann, M. M. 2012, *Earth and Planetary Science Letters*, 341, 48
- Hirschmann, M. M. 2022, *Geochim. Cosmochim. Acta*, 328, 221
- Hu, R., Bello-Arufe, A., Zhang, M., et al. 2024, *Nature*, 630, 609
- Ishii, T., Kojitani, H., & Akaogi, M. 2018, *Physics of the Earth and Planetary Interiors*, 274, 127
- Johansen, A. & Lambrechts, M. 2017, *Annual Review of Earth and Planetary Sciences*, 45, 359
- Johnstone, C. P., Bartel, M., & Güdel, M. 2021, *A&A*, 649, A96
- Kasting, J. F. 2014, *Treatise on Geochemistry*, 6, 157
- Katyal, N., Ortenzi, G., Lee Grenfell, J., et al. 2020, *A&A*, 643, A81
- Katz, R. F., Spiegelman, M., & Langmuir, C. H. 2003, *Geochemistry, Geophysics, Geosystems*, 4, 1073
- Kiehl, J. T. & Trenberth, K. E. 1997, *Bulletin of the American Meteorological Society*, 78, 197
- Kreidberg, L. & Stevenson, K. B. 2025, *Proceedings of the National Academy of Science*, 122, e2416190122
- Krissansen-Totton, J., Fortney, J. J., Nimmo, F., & Wogan, N. 2021, *AGU Advances*, 2, e00294
- Krissansen-Totton, J., Wogan, N., Thompson, M., & Fortney, J. J. 2024, *Nature Communications*, 15, 8374
- Kuwahara, H., Nakada, R., Kadoya, S., Yoshino, T., & Irifune, T. 2023, *Nature Geoscience*, 16, 461
- Lebrun, T., Massol, H., Chassefière, E., et al. 2013, *Journal of Geophysical Research (Planets)*, 118, 1155
- Lichtenberg, T., Bower, D. J., Hammond, M., et al. 2021, *Journal of Geophysical Research (Planets)*, 126, e06711
- Lichtenberg, T. & Miguel, Y. 2025, *Treatise on Geochemistry*, 7, 51
- Lichtenberg, T., Schaefer, L., Krissansen-Totton, J., et al. 2026, *The Planetary Science Journal*, 7, 108
- Lichtenberg, T., Schaefer, L. K., Nakajima, M., & Fischer, R. A. 2023, in *Astronomical Society of the Pacific Conference Series*, Vol. 534, *Protostars and Planets VII*, ed. S. Inutsuka, Y. Aikawa, T. Muto, K. Tomida, & M. Tamura, 907
- Lichtenberg, T., Shorttle, O., Teske, J., & Kempton, E. M.-R. 2025, *Science*, 390, eads3660
- Lin, Y., Ishii, T., van Westrenen, W., Katsura, T., & Mao, H.-K. 2024, *Nature Geoscience*, 17, 803
- Maurice, M., Tosi, N., & Hüttig, C. 2024, *Journal of Geophysical Research (Planets)*, 129, e2023JE008060
- May, E. M., MacDonald, R. J., Bennett, K. A., et al. 2023, *ApJ*, 959, L9
- McCanta, M. C., Elkins-Tanton, L., & Rutherford, M. J. 2009, *Meteoritics & Planetary Science*, 44, 725
- Mosenfelder, J. L., Asimow, P. D., Frost, D. J., Rubie, D. C., & Ahrens, T. J. 2009, *Journal of Geophysical Research (Solid Earth)*, 114, B01203
- Myhill, R., Frost, D. J., & Novella, D. 2017, *Geochim. Cosmochim. Acta*, 200, 408
- Nicholls, H. 2026, PhD thesis, University of Oxford
- Nicholls, H., Guimond, C. M., Hay, H. C. F. C., et al. 2025a, *MNRAS*, 541, 2566
- Nicholls, H., Lichtenberg, T., Bower, D. J., & Pierrehumbert, R. 2024, *Journal of Geophysical Research (Planets)*, 129, 2024JE008576
- Nicholls, H., Lichtenberg, T., Chatterjee, R. D., et al. 2025b, *Volatile-rich evolution of molten super-Earth L 98-59 d*
- Nicholls, H., Pierrehumbert, R., & Lichtenberg, T. 2025c, *The Journal of Open Source Software*, 10, 7726
- Nicholls, H., Pierrehumbert, R. T., Lichtenberg, T., Soucasse, L., & Smeets, S. 2024, *Mon. Not. R. Astron. Soc.*, 536, 2957
- Nikolaou, A., Katyal, N., Tosi, N., et al. 2019, *ApJ*, 875, 11
- O'Neill, H. S. C. & Eggins, S. M. 2002, *Chemical Geology*, 186, 151
- Owen, J. E. 2019, *Annual Review of Earth and Planetary Sciences*, 47, 67
- Pierrehumbert, R. & Gaidos, E. 2011, *ApJ*, 734, L13
- Pierrehumbert, R. T. 2010, *Principles of Planetary Climate*
- Raymond, C. A., Ermakov, A. I., Castillo-Rogez, J. C., et al. 2020, *Nature Astronomy*, 4, 741
- Rubie, D., Nimmo, F., & Melosh, H. 2015, 43
- Salvador, A., Avice, G., Breuer, D., et al. 2023, *Space Sci. Rev.*, 219, 51
- Salvador, A., Massol, H., Davaille, A., et al. 2017, *Journal of Geophysical Research (Planets)*, 122, 1458
- Schaefer, L., Pahlevan, K., & Elkins-Tanton, L. T. 2024, *Journal of Geophysical Research (Planets)*, 129, e2023JE008262
- Schaefer, L., Wordsworth, R. D., Berta-Thompson, Z., & Sasselov, D. 2016, *ApJ*, 829, 63
- Schlichting, H. E. & Young, E. D. 2022, 3, 127
- Sergeev, D. E., Mayne, N. J., Bendall, T., et al. 2023, *Geoscientific Model Development*, 16, 5601

- Shahar, G., Fei, Y., & Kessel, R. 2021, *Contributions to Mineralogy and Petrology*, 176, 83
- Shorttle, O., Jordan, S., Nicholls, H., Lichtenberg, T., & Bower, D. J. 2024, *ApJ*, 962, L8
- Sim, S. J., Hirschmann, M. M., & Hier-Majumder, S. 2024, *Journal of Geophysical Research (Planets)*, 129, e2024JE008346
- Solomatov, V. 2007, in *Evolution of the Earth*, ed. G. Schubert, Vol. 9, 91–119
- Sorbadere, F., Laurenz, V., Frost, D. J., et al. 2018, *Geochim. Cosmochim. Acta*, 239, 235
- Sossi, P. A., Burnham, A. D., Badro, J., et al. 2020, *Science Advances*, 6, eabd1387
- Sossi, P. A., Tollan, P. M. E., Badro, J., & Bower, D. J. 2023, *Earth and Planetary Science Letters*, 601, 117894
- Southworth, J., Mancini, L., Madhusudhan, N., et al. 2017, *AJ*, 153, 191
- Stagno, V. & Fei, Y. 2020, *Elements*, 16, 167
- Stothers, R. B. & Chin, C.-w. 1997, *ApJ*, 478, L103
- Suer, T.-A., Jackson, C., Grewal, D. S., Dalou, C., & Lichtenberg, T. 2023, *Frontiers in Earth Science*, 11, 1159412
- Swain, M. R., Estrela, R., Roudier, G. M., et al. 2021, *AJ*, 161, 213
- Teske, J. K., Wallack, N. L., Piette, A. A. A., et al. 2025, *A Thick Volatile Atmosphere on the Ultra-Hot Super-Earth TOI-561 b*
- Trønnes, R. G. 2000, *Lithos*, 53, 233
- Trønnes, R. G. & Frost, D. J. 2002, *Earth and Planetary Science Letters*, 197, 117
- Tsai, S.-M., Lee, E. K. H., Powell, D., et al. 2023, *Nature*, 617, 483
- Tsai, S.-M., Malik, M., Kitzmann, D., et al. 2021, *ApJ*, 923, 264
- Wade, J. & Wood, B. J. 2005, *Earth and Planetary Science Letters*, 236, 78
- Wagner, F. W., Plesa, A.-C., & Rozel, A. B. 2019, *Geophys. J. Int.*, 217, 75
- Walbecq, A., Samuel, H., & Limare, A. 2025, *Icarus*, 434, 116513
- Wang, H. S., Lineweaver, C. H., & Ireland, T. R. 2018, *Icarus*, 299, 460
- Watson, A. J., Donahue, T. M., & Walker, J. C. G. 1981, *Icarus*, 48, 150
- Wolf, A. S. & Bower, D. J. 2018, *Physics of the Earth and Planetary Interiors*, 278, 59
- Wordsworth, R. & Kreidberg, L. 2022, *ARA&A*, 60, 159
- Wordsworth, R. D., Schaefer, L. K., & Fischer, R. A. 2018, *AJ*, 155, 195
- Xie, L., Walter, M., Katsura, T., et al. 2024, *Earth and Planetary Science Letters*, 633, 118651
- Xue, Q., Bean, J. L., Zhang, M., et al. 2024, *ApJ*, 973, L8
- Young, E. D., Shahar, A., & Schlichting, H. E. 2023, *Nature*, 616, 306
- Zahnle, K. J. & Kasting, J. F. 1986, *Icarus*, 68, 462
- Zhang, H. L., Hirschmann, M. M., Cottrell, E., & Withers, A. C. 2017, *Geochim. Cosmochim. Acta*, 204, 83

Appendix

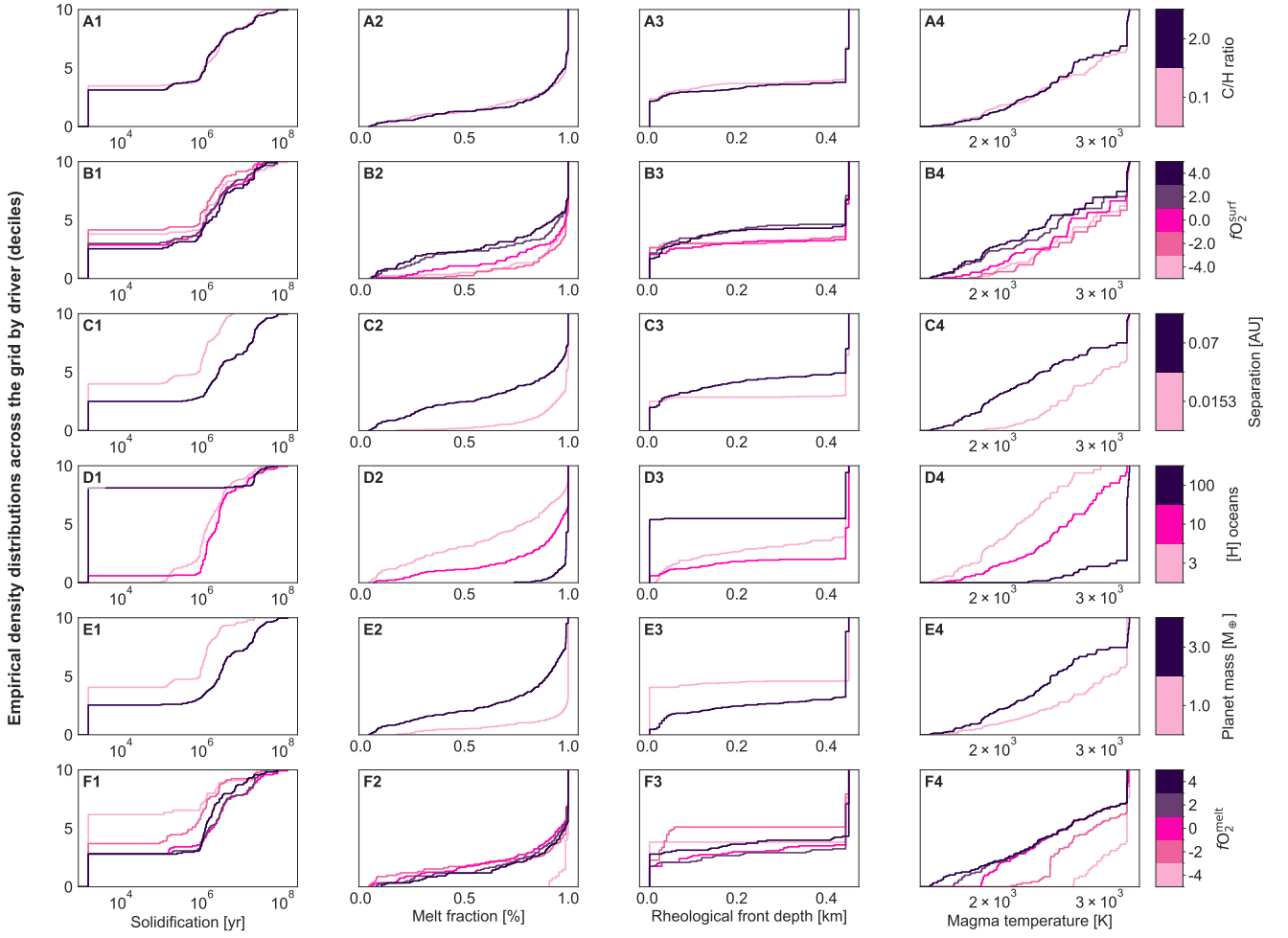


Fig. A.1. Empirical cumulative distribution function (ECDF) “impactogram” showing how each interior driver parameter shapes the distribution of key magma ocean outcomes across the full *PROTEUS* grid. Rows correspond to the six driver parameters explored in the grid: C/H ratio (row A), outgassing redox $\log f_{\text{O}_2}$ (row B), orbital separation (row C), bulk water budget expressed as H-oceans (row D), planet mass (row E), and melting-curve ΔIW shift (row F). Columns show the distribution of four interior outcomes: solidification time (col. 1), melt fraction at the end of the evolution (col. 2), rheological front depth (col. 3), and surface temperature (col. 4). For each driver, all simulations at the discrete grid levels are grouped and shown as ECDF curves. Colour intensity encodes the discrete values of each driver (colorbars at the right of each row), with darker colours representing higher grid values. Y-axis values (0-10) correspond to deciles of the cumulative distribution. This figure highlights how physical and chemical parameters imprint characteristic statistical signatures on magma ocean evolution. Together, these ECDF provide a compact summary of the sensitivity of magma ocean interior states to the multi-parameter driver space explored in this study.

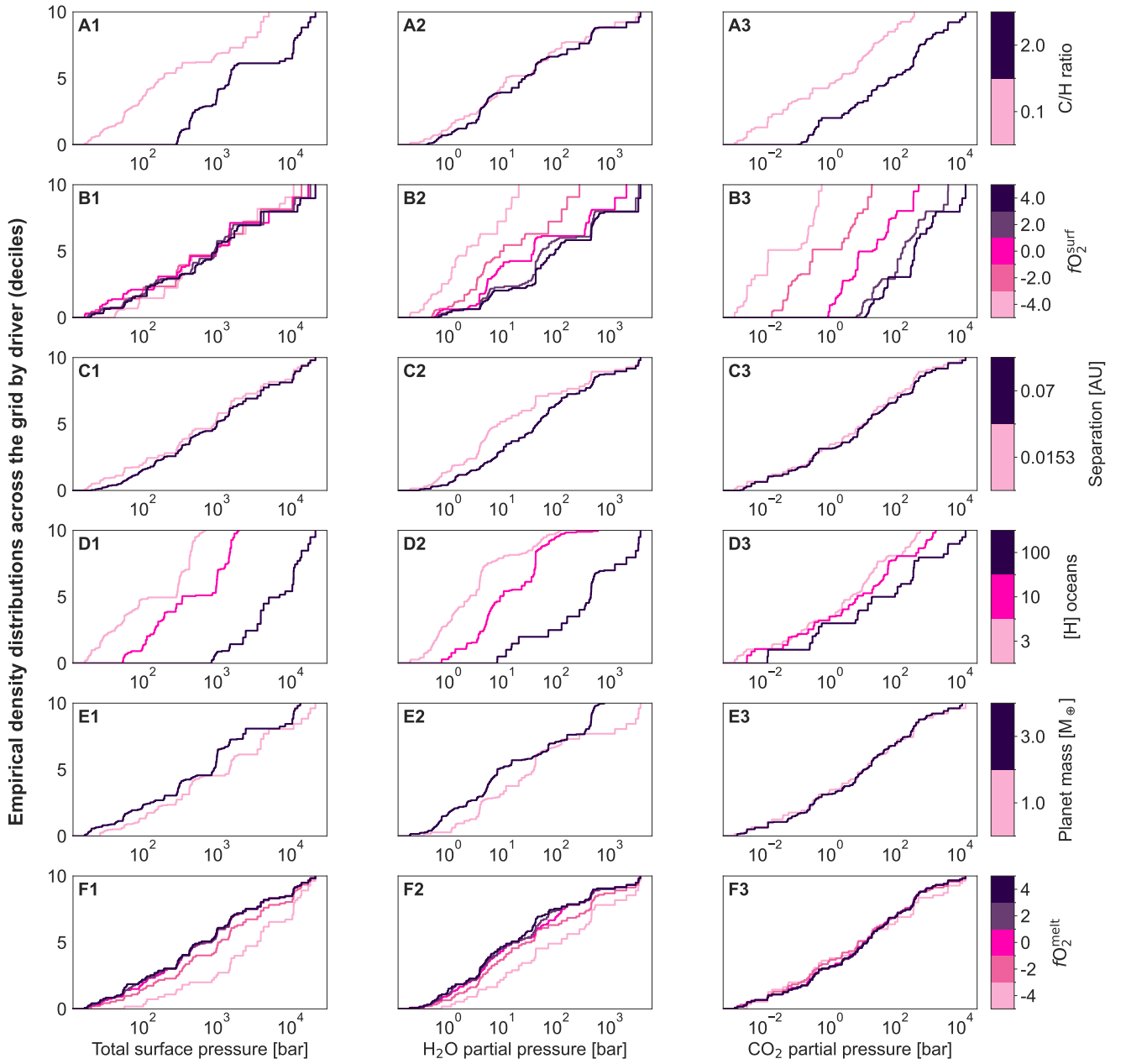


Fig. A.2. Same as Fig A.1 but illustrating how each interior driver parameter influences the distribution of atmospheric outcomes across the full PROTEUS grid. Columns show the resulting distributions for total Surface pressure (col 1), H_2O partial pressure (col 2), and CO_2 partial pressure (col 3).